Influence of radiation damage on Late Jurassic zircon from southern China: Evidence from *in situ* measurements of oxygen isotopes, laser Raman, U–Pb ages, and trace elements

Xiao-Lei Wang [a,b,*], Matthew A. Coble [c], John W. Valley [b], Xu-Jie Shu [a], Kouki Kitajima [b], Michael J. Spicuzza [b], Tao Sun [a]

[a] *State Key Laboratory for Mineral Deposits Research, School of Earth Science and Engineering, Nanjing University, Nanjing 210046, PR China*
[b] *WiscSIMS, Department of Geoscience, University of Wisconsin, 1215 W Dayton Street, Madison, WI 53706, USA*
[c] *Department of Geological and Environmental Sciences, Stanford University, 450 Serra Mall, Stanford, CA 94305-2115, USA*

ABSTRACT

The influence of radiation damage on chemical alteration and *in situ* elemental and isotopic analyses in zircons is evaluated in three ~155 Ma granites that are associated with W–Sn polymetallic deposits in the Nanling area of southern China. A combined approach is described using SEM imaging, laser Raman spectroscopy, and ion microprobe analysis of oxygen isotope ratios, U–Pb ages, and trace elements, including H. Domains within single zircons can be classified into two groups based on cathodoluminescence (CL) intensity and U–Th concentrations. Type-I are single crystals or clearly defined cores with bright CL, having U < 1400 ppm and Th < 800 ppm; type-II are rims surrounding type-I cores or single crystals with dark or intermediate CL-intensity and have 2100–30,000 ppm U and 900–6500 ppm Th. Both types of zircon display oscillatory zonation. Type-I zircons show a narrow range of $\delta^{18}O_{zircon}$ values (8.5–9.2‰), while type-II zircons have much greater variation of apparent $\delta^{18}O_{zircon}$ values (1.4–8.6‰). Relative to type-I, type-II zircons are characterized by elevated trace-element concentrations (including U, Th, rare earth elements, Y, Hf, Fe and Ti, $La_N > 10$), high cumulative α-dose and background-corrected $^{16}OH/^{16}O$, decreased Th/U and Hf/Yb ratios, and deviation in $^{206}Pb/^{238}U$ ages (up to 70 Ma) from the mean age (*ca.* 155 Ma) of type-I zircons. Moreover, laser Raman results show that type-II zircons have much broader FWHM (full width half maximum = 6.3–37.8 cm^{-1}) and decreased amplitudes for the ~1005 cm^{-1} Raman peak, indicating that they are affected by significant radiation damage. The Raman-measured preserved radiation damage ($D_\alpha^P = 0.01$–0.49×10^{15} α-decay events/mg) is less than the total alpha-dose ($D_\alpha^T = 0.1$–1.72×10^{15} α-decay events/mg) for each zircon of type-I and type-II with FWHM < 10 cm^{-1}, indicating that 30–80% of the total radiation damage experienced by most of these zircons has been annealed. We attribute the negative correlation of $\delta^{18}O$ *versus* U, Th, Y, Hf, La and cumulative α-dose for type-II zircons to open-system behavior resulting from radiation damage of the zircon crystal structure. We interpret type-II zircons to originally represent crystallization from a late-stage granite melt that was enriched in magmatic fluids and incompatible elements. The wide range and low $\delta^{18}O$ values recorded by most type-II zircon domains are the result of secondary alteration by fluids (perhaps hydrothermal) facilitated by radiation damage and open system chemical and isotopic exchange. This work shows that a combined approach using imaging, laser Raman and trace element analysis is effective for evaluating the influence of radiation damage and alteration of zircon. This protocol is necessary to evaluate the reliability of *in situ* oxygen isotopic and U–Pb ages. The $^{16}OH/^{16}O$ ratio is readily measured during SIMS analysis of oxygen isotopes and can be an effective parameter to monitor alteration of radiation-damaged domains in zircon.

© 2014 Elsevier B.V. All rights reserved.

1. Introduction

Over the last decade, *in situ* analyses of oxygen isotopes, U–Th–Pb isotopes, and trace elements in zircons have been widely used in radiometric dating, fingerprinting magmatic and sedimentary source contributions, characterizing crystallization processes, and understanding crustal evolution (*e.g.*, Peck et al., 2001; Valley et al., 2005; Belousova et al., 2006; Cavosie et al., 2007; Kemp et al., 2007; Harrison, 2009; Bouvier et al.,

* Corresponding author at: State Key Laboratory for Mineral Deposits Research, School of Earth Science and Engineering, Nanjing University, Nanjing 210046, PR China. Tel.: +86 2589680896; fax: +86 2589680700.
    E-mail address: wxl@nju.edu.cn (X.-L. Wang).

2012; Muñoz et al., 2012; Wang et al., 2013). However, it is necessary to evaluate the influence of radiation damage on these *in situ* isotopic and trace-element analyses before using them to discuss geological significance. It has been shown that radiation damage affects zircon oxygen isotope ratios (Valley et al., 1994; Peck et al., 2001; Valley, 2003; Pidgeon et al., 2013; Gao et al., 2014), U–Pb ages (Nasdala et al., 1998; Williams and Hergt, 2000; White and Ireland, 2012; Xu et al., 2012; Pidgeon et al., 2013; Gao et al., 2014; Steely et al., 2014) and trace elements (Marsellos and Garver, 2010; Bouvier et al., 2012), and care is needed to avoid radiation-damaged domains in zircon and to determine whether primary isotopic characteristics of the host magma are preserved. However, very few studies have quantitatively evaluated the extent to which *in situ* oxygen isotope ratios are modified in radiation-damaged zircons (Pidgeon et al., 2013; Gao et al., 2014; Valley et al., 2014), and a detailed evaluation of radiation damage by systematic imaging, *in situ* U–Pb ages, trace elements, and oxygen isotopes is still absent.

Zircon, nominally $ZrSiO_4$, is compositionally more complex than the formula implies. Major and trace elements including U^{4+}, Th^{4+}, Hf^{4+}, and Ti^{4+} substitute for Zr^{4+} in natural zircons because of the similarities in the ionic radii (Hoskin and Schaltegger, 2003), and other trace elements can also be incorporated into zircon structure by simple or coupled substitution, most notably rare earth elements (REE), Li, P and Y (Hoskin and Schaltegger, 2003; Fu et al., 2008; Ushikubo et al., 2008; Bouvier et al., 2012). Radioactive decay of U and Th are exploited for U–Th–Pb dating, however natural decay also causes internal radiation damage of the crystal structure which can accumulate over time (*e.g.*, Ewing et al., 2003; Farnan et al., 2003). The emission of one α-particle during decay causes the displacement of several hundred atoms, and the recoil of the radiogenic atom produces several thousand atomic displacements within the lattice (*e.g.*, Weber et al., 1994; Farnan and Salje, 2001; Fleischer, 2003; Marsellos and Garver, 2010). As a consequence, significant radiation damage can result in crystalline disorder, darker color, a decrease in density, volume expansion, and increased water content (Garver and Kamp, 2002; Ewing et al., 2003). If damage exceeds the first percolation point and amorphous domains form continuous pathways in zircon, then radiogenic lead mobility (loss or gain) can be facilitated by secondary alteration. Moreover, any open-system behavior (*e.g.*, element and isotope exchange) may significantly affect the measured isotope ratios and trace element concentrations.

Radiation damage in zircons has been previously evaluated by a wide range of techniques, including optics (decreased birefringence, expansion fractures), acid etching, X-ray diffraction, energy-dispersive X-ray spectrometry, infrared spectroscopy, nuclear magnetic resonance spectroscopy, transmission electron microscope, electron backscatter diffraction, cathodoluminescence (CL), electron backscatter diffraction, atom-probe tomography, molecular dynamic computer simulation, infrared laser Raman spectroscopy, oxygen isotope ratio, trace element composition, concordance of U–Pb ages, neutron irradiation, and hydrothermal alteration experiments (*e.g.*, Krogh and Davis, 1975; Sinha et al., 1992; Valley et al., 1994, 2014; Meldrum et al., 1998; Zhang et al., 2000; Trachenko et al., 2001; Ewing et al., 2003; Geisler et al., 2003a, 2005; Palenik et al., 2003; Nasdala et al., 2004, 2008; Cavosie et al., 2006; Marsellos and Garver, 2010). However, these techniques can be time-consuming, and many are destructive to the sample; they are not routinely carried out to evaluate radiation damage for *in situ* studies (see Cavosie et al., 2006). Furthermore, *in situ* trace element and isotopic (*e.g.*, U–Pb, oxygen) analyses by SIMS (secondary ion mass spectrometry) have high spatial resolution, small analytical volumes, and high abundance sensitivity, but these analyses are limited by the need to have matrix matched standard materials. Standardization of SIMS data by comparison of metamict samples to a crystalline zircon standard may not be valid, and such data should be used with caution. Therefore, it is important to find a practical way to evaluate the degree of radiation damage prior to or synchronous with *in situ* SIMS analyses of zircons.

In order to investigate the influence of radiation damage on *in situ* SIMS analyses in zircons, we present a case study of zircons from three representative Late Jurassic (~155 Ma) granites in the Nanling area of southeastern China (Fig. 1). Domains within single zircons are classified into two groups based on CL intensity and U–Th concentrations. Oxygen isotope ratios were measured in two types of zircon domains containing variable amounts of radiation damage, which we have evaluated based on spatially-correlated optics (transmitted and reflected light), CL imaging, laser Raman spectroscopy, U–Pb dating, and trace element analyses, including $^{16}OH/^{16}O$.

2. Sample description and analytical methods

Samples were collected from the Nanling area, located in the southern part of southeastern China (Cathaysia Block) (Fig. 1). Voluminous Mesozoic (especially Late Jurassic) granites are well exposed in the Nanling area, and are associated with the largest W–Sn ore field in the world (Zhou et al., 2006). The genetic relationship between granites and associated ore deposits remains unclear (*e.g.*, Zhu et al., 2008; Hu and Zhou, 2012). The three samples (07LZL-07, 07QLS-05-2, and 07YGX-01) analyzed in this study were selected from three small representative plutons (Laiziling, Qianlishan and Yaogangxian plutons, respectively) in the western part of the Nanling belt, which are dominantly associated with Sn–W, W–Sn and W ore deposits, respectively (Qi et al., 2012; Fig. 1a).

Shu et al. (2011, 2013) provided a detailed review of the geological history for the western Nanling area. Previous U–Pb dating of zircon by LA-ICP-MS and SHRIMP shows that the Laiziling, Qianlishan, and Yaogangxian granites formed at 151.8 ± 2.5 Ma to 155 ± 2 Ma (Shu et al., 2011; Zhu et al., 2011), 154.7 ± 2.1 Ma (Shu et al., 2011), and 152 ± 2 Ma to 158.4 ± 2.1 Ma (Li et al., 2011; Shu et al., 2013), respectively. The associated W–Sn deposits are interpreted to have formed contemporaneously with regional magmatism (153 ± 1 Ma to 155 ± 3 Ma) based on $^{40}Ar/^{39}Ar$ plateau ages of muscovite and phlogopite and Re–Os isochron dating of molybdenite (Peng et al., 2006; Yuan et al., 2007).

The samples analyzed in this study are fresh, without significant ore mineralization (Fig. S1). All three samples are peraluminous with aluminum saturation index values ranging from 1.07 to 1.08. Samples 07LZL-07 and 07QLS-05-2 are both biotite granites, with mineral assemblages dominated by quartz, plagioclase, biotite and K-feldspar, while 07YGX-01 is a two-mica granite. Sericitization of plagioclase was observed in all samples (Fig. S1). No pyroxene, garnet, cordierite or hornblende was identified in these rocks. The accessory minerals include zircon, Fe–Ti oxides, apatite and sphene.

After crushing and grinding of whole-rock samples, zircons were concentrated by heavy liquid and magnetic separation techniques, and hand selected for final purity. Zircons were mounted with the zircon standard KIM-5 ($\delta^{18}O = 5.09$‰ VSMOW; Valley, 2003) in epoxy and polished to mid-section. All grains were imaged by transmitted and reflected light on a petrographic microscope, and cathodoluminescence (CL) and backscattered electrons (BSE) on a scanning electron microscope (SEM) at UW-Madison to identify internal structure, inclusions, and physical defects prior to selecting locations for SIMS analytical pits. The mount was cleaned using distilled water and ethanol prior to gold-coating. Zircon grains were analyzed for oxygen isotope ratios ($\delta^{18}O_{zircon}$) *in situ* using the CAMECA IMS-1280 ion microprobe at the WiscSIMS Laboratory, UW-Madison, operated in multi-collection mode, following procedures described elsewhere (*e.g.*, Kita et al., 2009; Valley and Kita, 2009). Three masses (^{16}O, ^{18}O and $^{16}O^1H$) were analyzed simultaneously on Faraday cups (Orland, 2012). A $^{133}Cs^+$ primary ion beam (20 keV total impact voltage, 1.6–2.3 nA) was focused to an area of 8×9 μm on the sample surface. Total analytical time per spot was about 3.5 min, including 10 s of pre-sputtering, 120 s of automatic tuning of the secondary beam, and 80 s of analysis. After analysis, each pit was re-imaged using BSE/SE (secondary electrons) and any analyses that intersected significant cracks or inclusions are considered unreliable due to possible contamination. The oxygen isotope results
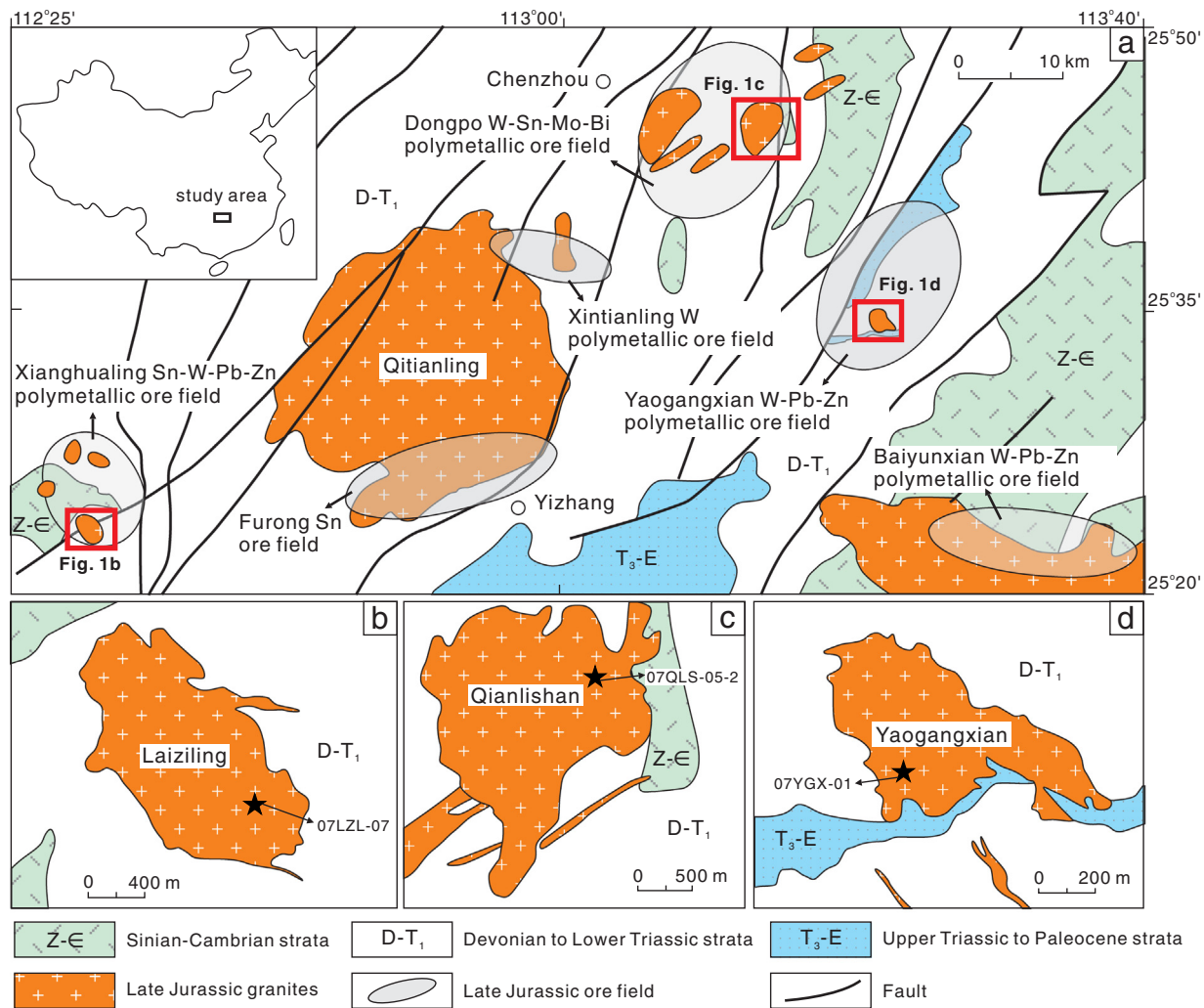
Fig. 1. Simplified geological map for studied granites in the Nanling area of southern China. (a) Western part of the Nanling area (modified after Peng et al., 2006). Inset boxes refer to geological sketch map of (b) the Laiziling Pluton (modified after Zhu et al., 2011), (c) the Qianlishan Pluton (modified after Shen et al., 1995), and (d) the Yaogangxian Pluton (modified after Li et al., 2011).

are shown in Table 1; detailed results and comments about pits are given in Table S1. As discussed by Kita et al. (2009) and Valley and Kita (2009), internal precision for a single spot (commonly <0.2‰) is not a good index of analytical quality for stable isotope ratios measured by SIMS. Therefore, the spot-to-spot precision of individual $\delta^{18}O$ analyses is estimated to be the two standard deviations (2SD) of the reproducibility of bracketing zircon standard KIM-5 (see Table S1). KIM-5 analyzed in this study show low and reproducible $^{16}OH/^{16}O$ ratios (0.00052 ± 0.00006; 1SD excluding 1 point). However, we do observe a slight increase of $^{16}OH/^{16}O$ for the KIM-5 over time, which may reflect slight variations in the vacuum quality and outgassing of mounts (see Table S1). To eliminate this effect, we calculated the corrected $^{16}OH/^{16}O$ for unknown analyses based on the average $^{16}OH/^{16}O$ of eight bracketing KIM-5 analyses (see notes of Table S1).

Following oxygen isotope analyses, the mount was lightly polished to remove the gold coating, cleaned, and then carbon-coated to image the pits by SEM. Laser Raman spectroscopy analyses were performed at the State Key Laboratory for Mineral Deposits Research, Nanjing University, using a Renishaw RM2000 laser Raman microscope coupled with an air-cooled CCD detector. Zircon laser Raman spectra were obtained from within the same domain as imaged in CL and located 2–5 μm away from oxygen isotope pits to avoid any damage imparted by SIMS analyses. Measurements were conducted at 23 °C with a laser power of 5 mW, and the instrumental resolution for all Raman spectral frequencies was better than 2 cm⁻¹. The beam was coupled with a

grating of 1800 grooves/mm, and the collection time was about 10 s. The lateral spatial resolution was about 1–2 μm. The amplitudes (intensities) and detected full width half maximum (FWHM) for different peaks (i.e., the bands related to the Si–O antisymmetric stretching vibrations) were obtained using the program Peakfit (v. 4.12). Because measured FWHM varies between different instruments, it is necessary to calculate the corrected FWHM values according to the Eq. (1) by Irmer (1985):

$$b = b_S \times \sqrt{1 - 2\left(\frac{S}{b_S}\right)^2} \qquad (1)$$

where b refers to the real FWHM (cm⁻¹); b_s refers to the detected FWHM; and S refers to the instrumental resolution (cm⁻¹). The laser Raman results are given in Table S2.

After laser Raman analyses, the polished block of zircons was cut from the original epoxy mount with a diamond wire saw and remounted in epoxy with zircon geochronology standard TEMORA-2 ($^{206}Pb/^{238}U$ age = 416.8 Ma; Black et al., 2004). The original polished zircon surfaces and orientations were maintained. The new mount was polished to remove the oxygen isotope analytical pits and to remove surface topography induced from remounting. Additional CL imaging was performed to check the CL patterns after polishing and locate analytical targets. Zircon U–Pb dating and analysis of 15 trace elements were performed

Table 1
Summary of ion-microprobe oxygen isotope, U–Pb age and Laser Raman FWHM results for Late Jurassic zircons from southern China.

Analysis	Type	CL intensity	δ^{18}O [a] (‰)	2σ SD (‰)	Amplitude [b] (counts)	FWHM[b] (cm^{-1})	Th (ppm)	U (ppm)	^{16}OH/^{16}O (/10^3) [c]	D$_a^c$-dose [d] (×10^{15}/mg)	^{206}Pb/^{238}U [e] (Ma)	1σ SD (Ma)
LZL-07_01-C	I	bright	8.8	0.2	63550	2.32	264	442	-0.01	0.22	148	1
LZL-07_01-R	II	dark	2.0	0.2	3705	6.30	4078	18751	11.54	9.57	84	3
LZL-07_02	I	bright	8.9	0.2	58320	2.24	233	464	0.01	0.21	152	2
LZL-07_03-C	I	bright	8.7	0.2	24550	1.46	208	470	0.02	0.22	156	3
LZL-07_03-R	II	dark	5.3	0.2	7552	33.11	1427	12030	5.10	5.40	142	5
LZL-07_04-C	I	bright	8.9	0.2	61810	5.49	400	967	-0.06	0.44	142	6
LZL-07_04-R	II	dark	6.8	0.2	6592	29.48	2296	8476	5.52	4.11	162	5
LZL-07_05-C	I	bright	8.8	0.2	86410	3.26	446	632	0.02	0.31	139	6
LZL-07_05-R1	II	dark	2.3	0.2	2108	16.43	5656	21064	8.76	10.7	122	1
LZL-07_05-R2	II	dark	1.1	0.3	3103	55.4	-	-	12.28	-	-	-
LZL-07_06-C	II	bright	6.4	0.2	97190	1.56	-	-	0.16	-	-	-
LZL-07_06-R1	II	dark	4.0	0.2	6110	17.83	-	-	12.92	-	-	-
LZL-07_06-R2	II	dark	1.8	0.3	1487	25.44	2371	22097	11.99	10.2	102	10
LZL-07_07-C	I	bright	8.7	0.3	23660	2.98	-	-	-0.03	-	-	-
LZL-07_07-R1	II	dark	6.6	0.3	2162	15.29	2807	9017	3.43	4.68	143	6
LZL-07_07-R2	II	dark	7.6	0.3	864	7.08	1639	7976	2.34	3.67	162	5
LZL-07_08-C	II	intermediate	8.4	0.3	15970	9.74	880	2624	0.14	1.22	159	3
LZL-07_08-R	II	dark	1.4	0.3	642	13.0	5383	32529	12.67	15.9	78	9
LZL-07_09-C	I	bright	8.9	0.3	3036	4.87	-	-	0.25	-	-	-
LZL-07_09-R	II	dark	4.5	0.3	0.4	10.20	-	-	7.12	-	-	-
LZL-07_10-C	I	bright	8.1	0.3	118500	2.75	-	-	0.10	-	-	-
LZL-07_10-R	II	dark	3.6	0.3	6354	14.99	-	-	7.90	-	-	-
LZL-07_11-C	I	bright	8.8	0.3	59760	3.16	254	452	0.01	0.20	152	4
LZL-07_11-R	II	dark	5.0	0.3	914	10.3	2048	9145	6.51	4.40	95	6
LZL-07_12-C	I	bright	8.6	0.3	11010	6.53	1002	5316	0.22	2.36	146	4
LZL-07_12-R	II	dark	5.8	0.3	1493	21.62	1532	9770	5.30	4.56	123	3
LZL-07_13-C	I	bright	8.9	0.3	234600	2.95	-	-	0.08	-	-	-
LZL-07_13-R	II	dark	5.3	0.3	5700	11.87	1166	9872	6.92	4.44	139	9
LZL-07_14-C	I	bright	8.7	0.3	11690	4.26	733	1622	0.04	0.79	152	3
LZL-07_14-R	II	dark	8.4	0.3	893	24.07	-	-	0.34	-	-	-
LZL-07_15-C	I	bright	8.9	0.3	3913	3.52	321	618	0.17	0.29	154	3
LZL-07_15-R	II	dark	4.3	0.3	1165	15.5	-	-	8.02	-	-	-
LZL-07_16-C	I	bright	8.8	0.3	10610	5.49	-	-	0.09	-	-	-
LZL-07_16-R	II	dark	4.9	0.3	1697	9.91	-	-	6.99	-	-	-
LZL-07_17-C	I	bright	8.6	0.3	-	-	809	1341	0.25	0.64	138	5
LZL-07_17-R	II	dark	4.6	0.3	-	-	1658	9371	8.11	4.68	118	3
YGX-1_01-C	I	bright	9.0	0.3	132400	1.39	140	196	0.11	0.10	160	3
YGX-1_01-R	II	dark	8.0	0.3	5355	6.45	3882	5959	1.33	3.04	166	4
YGX-1_02-C	II	intermediate	7.5	0.3	10620	5.36	-	-	0.52	-	-	-
YGX-1_02-R1	II	dark	6.4	0.3	1106	11.77	1111	14636	3.42	6.66	146	4
YGX-1_02-R2	II	dark	6.4	0.3	740	10.46	-	-	11.23	-	-	-
YGX-1_03-C	II	intermediate	8.4	0.3	1302	6.47	1320	3487	0.22	1.60	161	3
YGX-1_03-R1	II	dark	6.8	0.3	592	19.3	3216	29183	14.51	14.0	94.1	3
YGX-1_03-R2	II	dark	6.1	0.3	-	-	-	-	14.46	-	-	-
YGX-1_04-C	II	intermediate	8.5	0.3	13630	6.99	1024	2754	0.20	1.29	158	4
YGX-1_04-R	II	dark	7.8	0.3	2741	6.83	-	-	0.40	-	-	-
YGX-1_05-C	I	bright	9.2	0.3	77120	3.69	162	229	0.12	0.11	162	14
YGX-1_05-R	II	dark	8.1	0.3	2318	17.04	3344	7114	1.01	3.37	163	14
YGX-1_06-C	I	bright	9.0	0.4	107000	2.08	422	350	-0.01	0.19	156	5
YGX-1_06-R	II	dark	8.3	0.4	4691	9.49	1427	7671	0.42	3.40	163	4
YGX-1_07-C	I	bright	8.7	0.4	2134	4.29	900	1563	0.02	0.75	158	3
YGX-1_07-R	II	dark	7.2	0.4	736	23.74	1665	4129	1.84	1.89	155	6
YGX-1_08	I	bright	8.6	0.4	7822	5.74	1796	2721	-0.05	1.30	160	4
YGX-1_09-C	I	bright	8.5	0.4	173200	2.01	416	539	-0.05	0.26	145	3
YGX-1_09-R	II	dark	6.5	0.4	5717	6.53	2495	16675	4.48	7.20	134	5
YGX-1_10-C	II	intermediate	8.2	0.4	18460	6.26	2259	2682	0.31	1.37	154	6
YGX-1_10-R1	II	dark	4.8	0.4	1876	9.72	3753	16307	9.13	7.49	127	7
YGX-1_10-R2	II	dark	8.3	0.3	1906	10.14	-	-	6.89	-	-	-
YGX-1_11-C	II	intermediate	8.8	0.4	1156	12.33	2342	9069	0.13	4.48	132	7
YGX-1_11-R	II	dark	7.4	0.4	1256	8.3	-	-	7.29	-	-	-
YGX-1_12	II	dark	7.7	0.4	490	8.65	3114	12588	1.00	5.65	126	15
YGX-1_13	II	intermediate	8.6	0.4	19930	8.08	1335	3224	0.31	1.49	161	2
YGX-1_14-C	II	intermediate	8.1	0.4	16420	6.54	-	-	0.38	-	-	-
YGX-1_14-R	II	dark	7.1	0.4	1034	18.2	-	-	4.29	-	-	-
YGX-1_15-C	II	intermediate	8.6	0.4	12460	6.98	1360	3560	0.12	1.68	155	3
YGX-1_15-R	II	dark	6.5	0.4	459	8.1	-	-	0.66	-	-	-
YGX-1_16-C	II	intermediate	8.2	0.4	4074	7.04	-	-	0.18	-	-	-
YGX-1_16-R	II	dark	6.4	0.4	677	37.8	2285	19017	2.52	9.04	144	1
YGX-1_17-C	II	intermediate	8.3	0.4	2908	16.13	1582	3628	0.40	1.72	151	7
YGX-1_17-R	II	dark	4.7	0.4	602	26.89	5546	29786	11.12	14.7	135	16
QL5-2_01	I	bright	9.2	0.4	11380	5.89	2901	1606	-0.06	0.93	126	9
QL5-2_02-C	II	intermediate	8.2	0.4	2561	6.49	-	-	1.58	-	-	-
QL5-2_02-R1	II	dark	4.2	0.4	1559	27.43	1823	17371	4.21	7.89	299	18

(continued on next page)

Table 1 (continued)

Analysis	Type	CL intensity	$\delta^{18}O$ [a] (‰)	2σ SD (‰)	Amplitude [b] (counts)	FWHM [b] (cm^{-1})	Th (ppm)	U (ppm)	$^{16}OH/^{16}O$ (/10^3) [c]	D_s^C-dose [d] ($\times 10^{15}$/mg)	$^{206}Pb/^{238}U$ [e] (Ma)	1σ SD (Ma)
QL5-2_02-R2	II	dark	6.1	0.3	2623	35.64	-	-	5.03	-	-	-
QL5-2_03-C	I	bright	8.4	0.4	77890	3.53	-	-	0.26	-	-	-
QL5-2_03-R	II	dark	6.5	0.4	2851	9.69	1873	8561	0.31	3.94	164	5
QL5-2_04-C	I	bright	8.9	0.4	3947	6.78	-	-	-0.02	-	-	-
QL5-2_04-R	II	dark	8.2	0.4	700	7.70	-	-	0.53	-	-	-
QL5-2_05-C	I	bright	8.9	0.4	2294	11.54	483	1500	-0.05	0.67	152	3
QL5-2_05-R1	II	dark	5.8	0.4	1177	10.7	-	-	12.72	-	-	-
QL5-2_05-R2	II	dark	7.9	0.3	923	10.73	2101	16113	1.23	7.40	122	8
QL5-2_06-C	II	intermediate	6.4	0.4	59760	3.83	-	-	0.64	-	-	-
QL5-2_06-R	II	dark	1.9	0.4	2064	7.92	-	-	8.59	-	-	-
QL5-2_07	I	bright	8.7	0.4	2110	6.44	448	1638	-0.03	0.73	146	6
QL5-2_08-C	I	bright	9.0	0.4	65250	4.43	-	-	-0.08	-	-	-
QL5-2_08-R	II	dark	7.6	0.4	2261	13.52	-	-	1.42	-	-	-
QL5-2_09-C	I	bright	8.7	0.3	10770	6.18	-	-	-0.01	-	-	-
QL5-2_09-R	II	dark	7.3	0.3	910	11.83	-	-	1.29	-	-	-
QL5-2_10-C	II	intermediate	8.1	0.3	27500	8.61	-	-	0.55	-	-	-
QL5-2_10-R1	II	dark	8.5	0.3	7030	8.33	-	-	0.22	-	-	-
QL5-2_10-R2	II	dark	8.2	0.3	2848	10.83	-	-	0.50	-	-	-
QL5-2_11-C	I	bright	9.0	0.3	42790	6.83	-	-	0.02	-	-	-
QL5-2_11-R	II	dark	5.8	0.3	3677	7.38	-	-	2.58	-	-	-
QL5-2_12-C	I	bright	8.7	0.3	3564	13.49	-	-	2.39	-	-	-
QL5-2_12-R	II	dark	5.5	0.3	651	17.2	-	-	11.47	-	-	-

- not determined.
[a] The oxygen isotopes values are relative to VSMOW ;
[b] The amplitudes and FWHM results are for the B_{1g} band;
[c] background corrected (see text).
[d] α-dose was calculated based on the formula (2) in the text;
[e] The ages are corrected by $^{207}Pb_c$;

on the SHRIMP-RG ion microprobe that is co-maintained by the U.S. Geological Survey and Stanford University. The run table included $^{48}Ti^+$, $^{49}Ti^+$, $^{56}Fe^+$, $^{89}Y^+$, $^{139}La^+$, $^{140}Ce^+$, $^{146}Nd^+$, $^{147}Sm^+$, $^{153}Eu^+$, $^{155}Gd^+$, $^{163}Dy^{16}O^+$, $^{166}Er^{16}O^+$, $^{172}Yb^{16}O^+$, $^{90}Zr_2^{16}O^+$, $^{180}Hf^{16}O^+$, $^{204}Pb^+$, background measured at 0.046 mass units above the $^{204}Pb^+$ peak, $^{206}Pb^+$, $^{207}Pb^+$, $^{208}Pb^+$, $^{232}Th^+$, $^{238}U^+$, $^{232}Th^{16}O^+$, $^{238}U^{16}O^+$, and $^{238}U^{16}O_2^+$. Analyses of TEMORA-2 were performed after every four unknown analyses. A primary O_2^- ion beam (3.9–5.0 nA) was focused to a spot size of about 14×17 μm. All peaks were measured on a single ETP® discrete-dynode electron multiplier 4 times (4 scans through the mass sequence from $^{48}Ti^+$ through $^{238}U^{16}O_2^+$). The duration of each analysis was about 17 min, including 2.5 min for raster and primary and secondary tuning. Trace element concentrations (including U and Th) were calibrated using an internal zircon standard MADDER (3435 ppm U) which is referenced to the composition of zircon reference material MAD-green (Barth and Wooden, 2010). U–Pb ages and trace element concentrations were calculated and plotted using Squid 2.51 (Ludwig, 2009) and Isoplot 3.76 (Ludwig, 2012) programs in Excel. U–Th–Pb isotope and trace element (Table S3) data for individual spots are given with 1SD uncertainty. The reported $^{206}Pb/^{238}U$ model ages were corrected for common Pb using ^{207}Pb based on a model Pb composition from Stacey and Kramers (1975). After U–Pb analysis, each pit was re-imaged using BSE/SE and trace element concentrations for any analyses that intersected significant cracks or inclusions were discarded due to possible contamination (Table S3).

3. Results

3.1. CL and BSE textures

The separated zircons are pink in color and semi-transparent to opaque. They are generally prismatic with width/length ratios of 1:2 to 1:3. The Laiziling and Yaogangxian zircons are relatively large (100–150 μm c-axis lengths), while the Qianlishan zircons are typically smaller (60–100 μm in length). Representative CL and BSE images are shown in Fig. 2; detailed CL images for each analyzed zircon are presented in Fig. S2. Both the BSE and CL images show rhythmic zonation (Fig. 2),

although a few zircons also show patchy zoning in some areas (Fig. 2i). These textures are consistent with zircon domains that are not significantly affected by later alteration. About 30–50% of the imaged zircons show bright oscillatory CL in the interior and a dark oscillatory CL in the rim (Figs. 2 and S2). We named these distinct interiors as "CL defined cores" followed Wang et al. (2013). They are interpreted to be magmatic zircons (see the Discussion section), which are distinctly different from old cores inherited as xenocrysts. Contacts between bright CL cores and dark rims are often, but not always, sharp and parallel to the oscillatory zonation (Fig. 2). Crenulated boundaries between bright and dark CL zones are also observed in some grains. A minority of zircons show entirely dark CL or completely bright CL without contrastive CL-intensity rims. In this work, we group the zircon domains with bright CL as type-I and domains with dark CL as type-II. Some zircons (especially in sample 07YGX-01) show intermediate CL-intensity in the core and dark CL in the rim with parallel zonation (Fig. S2). These zircon domains with intermediate CL-intensity are also considered type-II based on their elevated Th and U concentration (see below).

3.2. Oxygen isotopes

Type-I zircons show a narrow range in $\delta^{18}O$ from 8.5‰ to 9.2‰ (Table 1), with an average of 8.8 ± 0.3‰ (2SD). In contrast, type-II zircons show a large variation in $\delta^{18}O$ (1.4–8.6‰) (Table 1; Fig. 3a). Some type-II zircon domains (especially the intermediate-intensity CL domains from 07YGX-01) have $\delta^{18}O$ values similar to those of type-I zircons, but most of the dark-CL type-II domains have lower $\delta^{18}O$ values (Fig. 3a). The difference between oxygen isotope ratios of type-I versus type-II zircon domains can be seen within individual zoned grains (Fig. 2; Table 1). In particular, type-II domains within the same zircon grain can vary by up to 3.5‰. For example, two analyses were obtained from the rim (type-II domain) of grain #LZL-07_06 and they gave $\delta^{18}O$ of 4.0‰ and 1.8‰, respectively (Table 1; Fig. S2).

Values of $^{16}OH/^{16}O$ were analyzed by multi-collector simultaneously with the oxygen isotope ratios and from the same analytical volume. These values are not calibrated to ppm H because we are not aware of a homogeneous H standard for zircon. KIM-5 has low amounts of
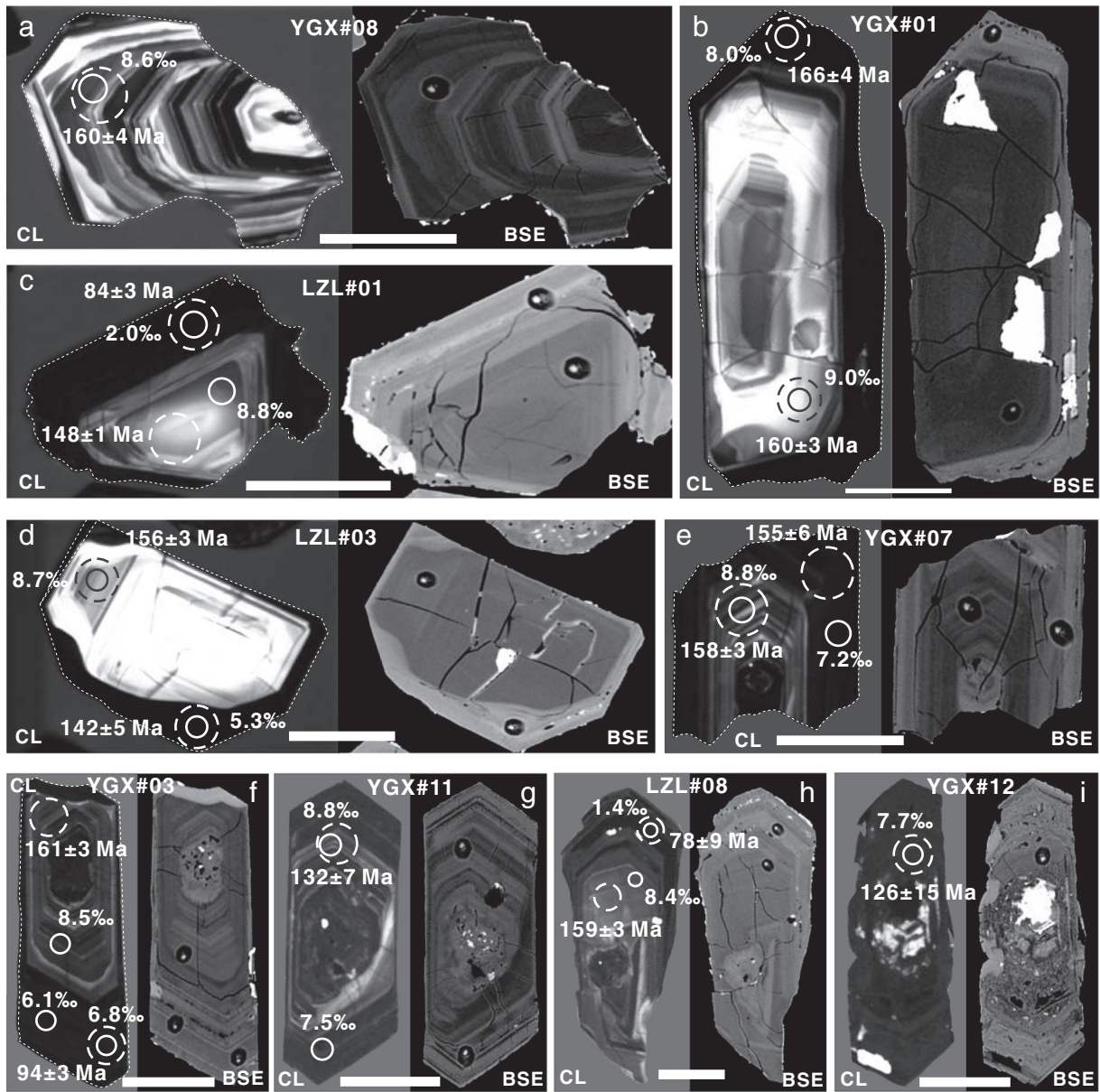
Fig. 2. Representative cathodoluminescence (CL) and backscattered electron (BSE) images for zircons in this study. For each inset image, CL is on the left and BSE is on the right. (a) Zircon (type-I) with bright CL. Note that a few dark-CL bands occur within the bright-CL bands. These dark bands might be damaged domains that should be avoided in oxygen isotope and U–Pb analyses. (b–d) Zircons with a bright CL core (type-I) surrounded by a dark rim (type-II). (e–h) Zircons with an intermediate intensity CL core interpreted to be type-II zircon surrounded by a darker rim (also type-II). (i) Zircons with dark CL (type-II) but without obvious regular cores. Note that some bright and dark irregular cores in the zircons are products of radiation damage (Corfu et al., 2003). The analysis pits, results of SIMS $\delta^{18}O_{VSMOW}$ (‰, solid circle), SHRIMP-RG U–Pb ages, and 1σ error (Ma, dashed circle) are indicated. Scale bar is 50 μm for each image. The white spots along zircon margins and irregular areas within zircon pits imaged in the BSE images are artifacts (residual gold coat from SIMS from SIMS analyses).

radiation damage and is H-poor. Each measured value of $^{16}OH/^{16}O$ is background corrected using KIM-5, providing a relative index of the amount of H in the zircon domain that was analyzed. The most likely source of H in zircon is from OH and water in radiation damaged domains of zircon. Type-I zircons generally show corrected $^{16}OH/^{16}O$ lower than 0.0006; except QL5-2_02-C and QL5-2_12-C at 0.0016 and 0.0024, respectively (Fig. 3b, Table S1). In contrast, type-II zircons have variable and elevated $^{16}OH/^{16}O$ values (0.0001–0.0145; Table S1; Fig. 3b).

3.3. Laser Raman spectroscopy

The laser Raman results also show significant variations for the two types of zircon. Laser Raman spectra for most type-I zircons are characterized by strong B_{1g} (v_3 [SiO_4]), A_{1g} (v_2 [SiO_4]) and E_g (I [Si–Zr]) bands,

with peaks at ~1005 cm^{-1}, ~435 cm^{-1}, and ~355 cm^{-1}, respectively; similar to typical synthetic zircons (e.g., Marsellos and Garver, 2010). In contrast, there is a decrease in peak intensity (amplitude) and an increase in peak width (FWHM) for the B_{1g} band (~1005 cm^{-1}) of type-II zircons (Table S2; Fig. 3c). For example, type-I zircons have FWHM B_{1g} band values of 1.4–6.4 cm^{-1} (with #QLS-5C at 11.5 cm^{-1}; Table S2), while type-II zircons show elevated values of 6–38 cm^{-1} (Fig. 3c; Table S2). Moreover, a shift (commonly decrease) in B_{1g} band is common for type-II zircons; the B_{1g} peak is lower than 1000 cm^{-1} for about two-thirds of type-II analyses (Table S2).

3.4. U–Pb dating

All U–Pb analyses plot on or near the Concordia line (Fig. 4a, c, e), although 6 of 53 analyses have high common Pb (>20%), and type-II
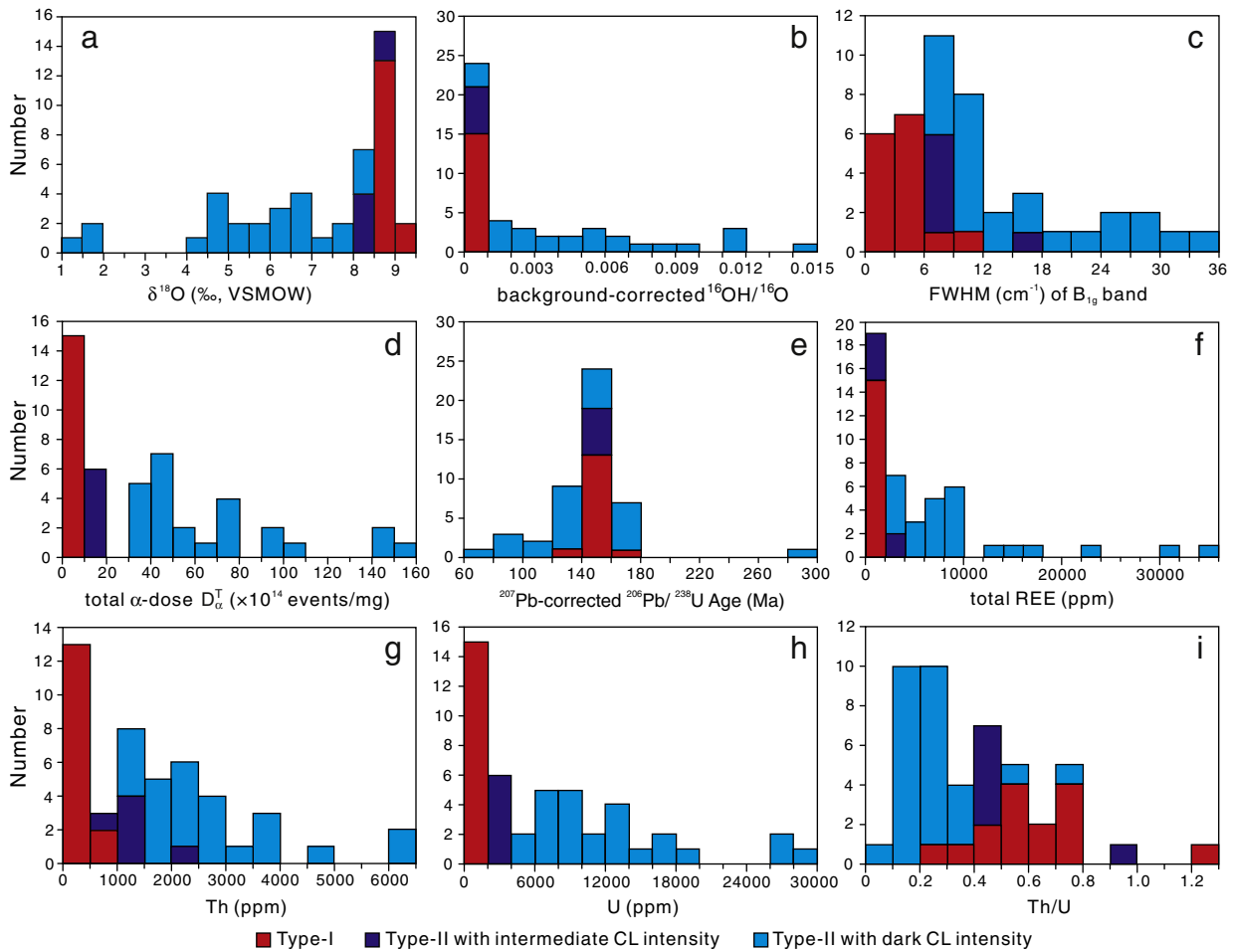
Fig. 3. Histograms of $\delta^{18}O$ (a), $^{16}OH/^{16}O$ (b), FWHM (c), total cumulative α-dose D_α^T (d), U–Pb ages (e), total REE (f), Th (g), U (h) and Th/U (i) for type-I and type-II zircons from the Nanling area, southern China.

analyses tend to have large uncertainties (Table S3). The low-U analyses (type-I) and some (n = 6) of the high-U (type-II) domains of 07YGX-01 are concentrated around 150 Ma, yielding weighted-average ^{207}Pb-corrected $^{206}Pb/^{238}U$ ages of 149.5 ± 2.9 Ma (n = 9, 2SE, MSWD = 2.66; Fig. 4b) for 07LZL-07, 150.9 ± 5.4 Ma (n = 2, 2SE, MSWD = 0.97; Fig. 4d) for 07QLS-05-2, and 157.2 ± 3.0 Ma (n = 12, 2SE, MSWD = 1.88; Fig. 4f) for 07YGX-01. These age results are consistent with the zircon laser-ICP-MS U–Pb ages reported by Shu et al. (2011, 2013).

Type-II zircons generally yield younger $^{206}Pb/^{238}U$ ages than type-I zircons, with ages ranging from ~80 Ma to ~160 Ma, with the exception of one grain at ~300 Ma (QLS-2R1; Figs. 3e, 4d). The deviation in age generally correlates with increasing U (Fig. 4) and Th concentrations (discussed below), but does not correlate with common Pb (i.e., $^{206}Pb/^{204}Pb$). Analyses with relatively high U and Th concentrations do not necessarily show high common Pb, but the uncertainties in $^{206}Pb/^{238}U$ and $^{207}Pb/^{206}Pb$ are generally larger (Table S3).

3.5. Trace elements

The two types of zircon domains are clearly distinguished by trace element compositions. Type-I zircons have U and Th concentrations lower than 1400 ppm and 800 ppm, respectively, whereas type-II zircons have relatively high U (>2100 ppm) and Th (>900 ppm) (Figs. 3g, h, 5a; Table S3). Moreover, type-I zircons have low REE (including La), low Hf and Fe concentrations, and high Ce/Ce*, whereas

type-II zircons show strongly elevated concentrations in these elements and decreased Ce/Ce* ratios (Figs. 3f, 5a–c, 6). Some type-II zircons have flat LREEs characterized by elevated La. About 40% of type-II zircons show high Ti concentrations (up to 480 ppm), but the majority are similar to type-I zircons (Fig. 5d), ranging from 5 to 17 ppm. In addition, type-I and type-II zircons generally have different Th/U (0.29–1.28 vs. 0.09–0.93) and Hf/Yb (14–60 vs. 1.3–24) ratios (Table S3; Figs. 3i, 5f), and most type-II zircons do not follow the fractional crystallization trends defined by type-I zircons (Fig. 5e, f). Both zircon types show significant negative Eu anomalies. However, type-II zircons with intermediate CL-intensity are similar to type-I $\delta^{18}O$ values and REE patterns (Fig. 6c).

4. Discussion

4.1. Quantifying radiation damage of type-II zircons

Type-II zircons and zircon domains show U concentrations over 2100 ppm and 75% are >5000 ppm (Table S3; Fig. 3h), which is higher than most natural magmatic zircon grains ([U] = 100–500 ppm; Marsellos and Garver, 2010) or the altered zircons ([U] = 800–5000 ppm) from the Acasta Gneiss Complex of northwestern Canada (Rayner et al., 2005). In addition, type-II zircons also show high Th concentrations (Fig. 3g). The high-U and Th concentrations will cause radiation damage that can make zircons darker in color, as observed under optical microscope. Radiation damage leads to open-
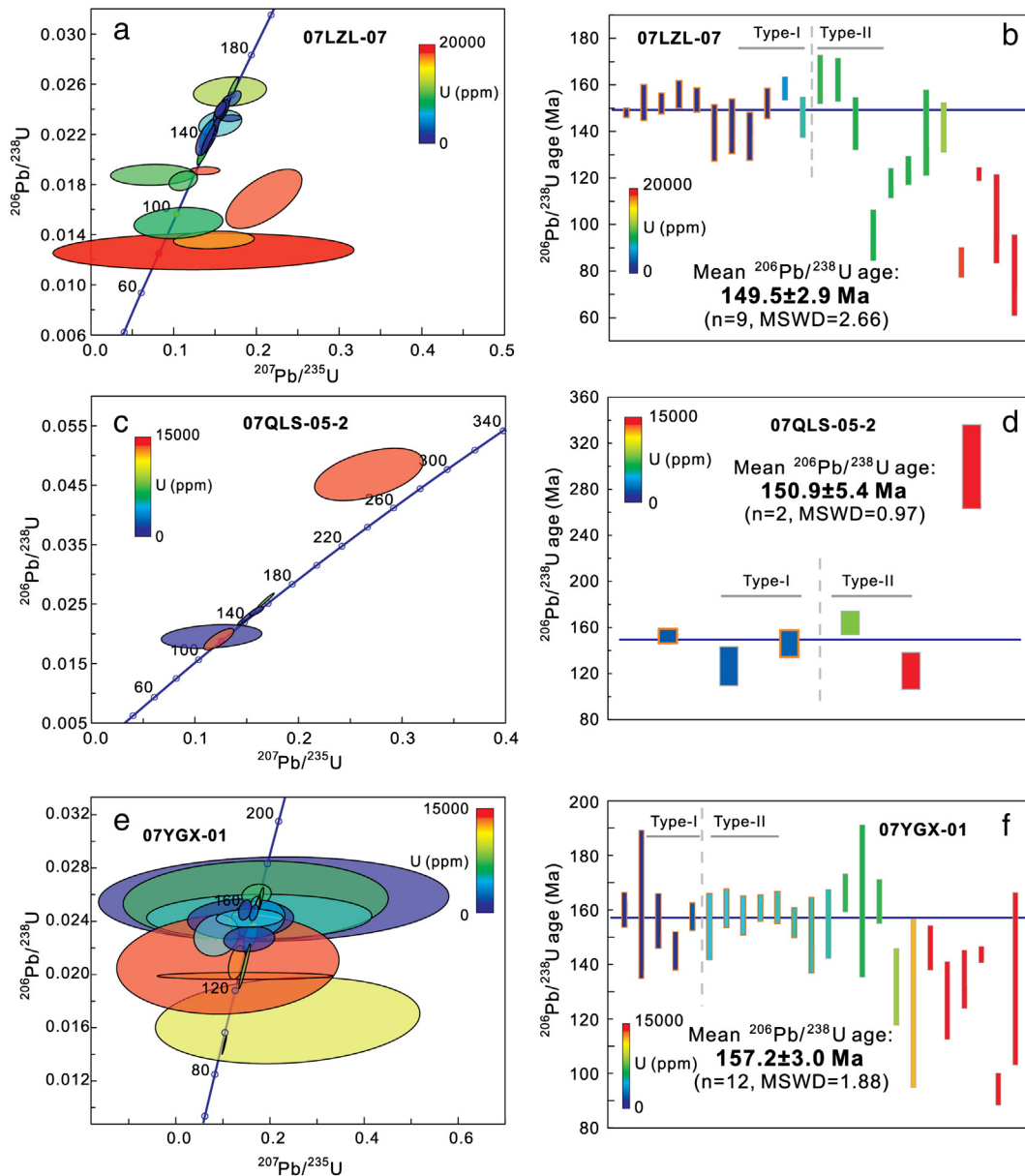
Fig. 4. U–Pb Concordia plots and calculated $^{206}Pb/^{238}U$ ages for the Late Jurassic zircons from Nanling area of southern China. (a–b) 07LZL-07; (c–d) 07QLS-05-2; (e–f) 07YGX-01. The U concentration variations for each sample are also indicated by fill color. Analyses included in calculating weighted mean ages are surrounded by orange boxes (error ellipses and bars are shown as 1σ). (For interpretation of the references to color in this figure legend, the reader is referred to the web version of this article.)

system exchange that facilitates incorporation of some REEs and other trace elements (*e.g.*, Y, Fe and Ti) in type-II zircons (Figs. 4 and 5; Table S3). For example, iron does not fit readily into either the Si or Zr-sites in zircon and averages 1.2 ppm in type-I *vs.* 830 ppm in the damaged type-II zircons (Fig. 5b; Table S3). In cases where Ti has been added after crystallization of a zircon, the calculation of temperature by Ti-in-zircon thermometer (Watson et al., 2006) is not appropriate.

Given a similar thermal history, zircons with higher U and Th show more radiation damage than those with lower U–Th concentrations (Marsellos and Garver, 2010). It has been shown that α-recoil is chiefly responsible for the radiation damage of zircon (*e.g.*, Ewing et al., 2003; Nasdala et al., 2004; Marsellos and Garver, 2010) and the alpha dose (α-decay events/mg) can be calculated (assuming no annealing) using Eq. (2) (Nasdala et al., 2001; Palenik et al., 2003).

$$D_\alpha^T = 8N_1[\exp(\lambda_1 t)-1] + 7N_2[\exp(\lambda_2 t)-1] + 6N_3[\exp(\lambda_3 t)-1] \quad (2)$$

where D_α^T refers to the total dose in α-decay events/mg; N_1, N_2, and N_3 are the present numbers of ^{238}U, ^{235}U, and ^{232}Th, respectively, in atoms/mg; λ_1, λ_2, and λ_3 are the decay constants for ^{238}U, ^{235}U, and ^{232}Th, respectively, in years^{-1}; and t is the age of the zircon. Type-II zircons from the ~155 Ma Nanling granites show D_α^T of 1.2–15.7 × 10^{15} α-decay events/mg and 75% show $D_\alpha^T > 8 \times 10^{15}$ α-decay events/mg (Table 1), belonging to middle- to high-degree of radiation damage in zircon (Murakami et al., 1991) if not annealed. In contrast, most type-I zircons show D_α^T lower than 1×10^{15} α-decay events/mg (Table 1), indicating a low-degree of radiation damage.

Note that the total dose represents the maximum amount of radiation damage that might be present in a zircon. Damage is at least partly annealed in most zircons at temperatures above 200–300 °C; the rate of annealing depends on temperature, time and fluids (Ewing et al., 2003). It is difficult to know the actual radiation damage preserved in zircon without spectroscopic measurements. Since there is a close relationship between radiation damage preserved in a zircon and Raman spectra
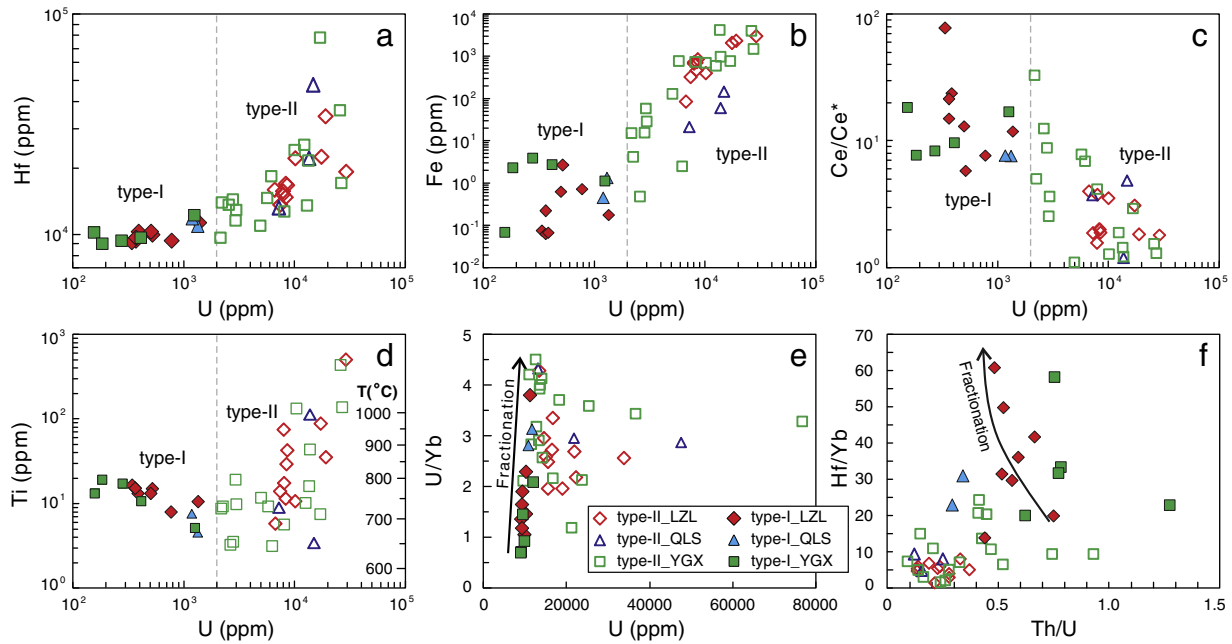
Fig. 5. Variation diagrams for the trace elements and element ratios of Late Jurassic zircons from Nanling area of southern China. (a) Hf *vs.* U; (b) Fe *vs.* U; (c) Ce/Ce* *vs.* U; (d) Ti *vs.* U. Temperature (Watson et al., 2006) on the right y-axis is calculated with Si and Ti activities to unity, but [Ti] is elevated by subsolidus alteration in many type-II zircons; (e) U/Yb *vs.* U; (f) Hf/Yb *vs.* Th/U. Type-I (solid symbols) and type-II (open symbols) zircons show consistent differences in trace element concentrations and Ce/Ce*, Th/U, U/Yb and Hf/Yb ratios. The fractionation trends in Fig. 5e and f schematically represent type-I zircons, and contrast the trends (or fields) for radiation damaged type-II zircons.

(*e.g.*, Nasdala et al., 2001, 2008; Ewing et al., 2003; Marsellos and Garver, 2010), Nasdala et al. (2001) suggested an empirical equation:

$$\text{FWHM}\ \left(\text{cm}^{-1}\right) \approx 1.2 + 1400 \times D_{\alpha}^{P}\left(10^{15}/\text{mg}\right) \qquad (3)$$

where FWHM is for the B_{1g} band and D_{α}^{P} refers to the preserved cumulative α-decay events/mg. Note that Eq. (3) is only meaningful for less radiation-damaged zircons (FWHM < 20 cm^{-1}) and cannot be applied to highly damaged zircons (Nasdala et al., 2001). One possible reason is that in highly damaged zircons the FWHM of B_{1g} band could expand

irregularly, leading to deviation from the correlation with D_{α}^{P}, *i.e.* not following the trend defined by Eq. (3). Moreover, the FWHM is difficult to measure since the peak may have shifted. For this study, there is a rough positive correlation only for analyses with FWHM lower than 10 cm^{-1} and D_{α}^{T} lower than 2×10^{15} α-decay events/mg (Fig. 7a), which suggests only that the zircon domains within these ranges are meaningful to calculate D_{α}^{P} using Eq. (3). Note that 2×10^{15} α-decay events/mg is also the first percolation point for crystalline zircon (Ríos et al., 2000; Ewing et al., 2003). All type-I zircons (except QL5-2_05-C; Table 1) fall within the ranges defined by FWHM < 10 cm^{-1} and $D_{\alpha}^{T} < 2 \times 10^{15}$ α-decay events/mg, while only five analyses of type-II
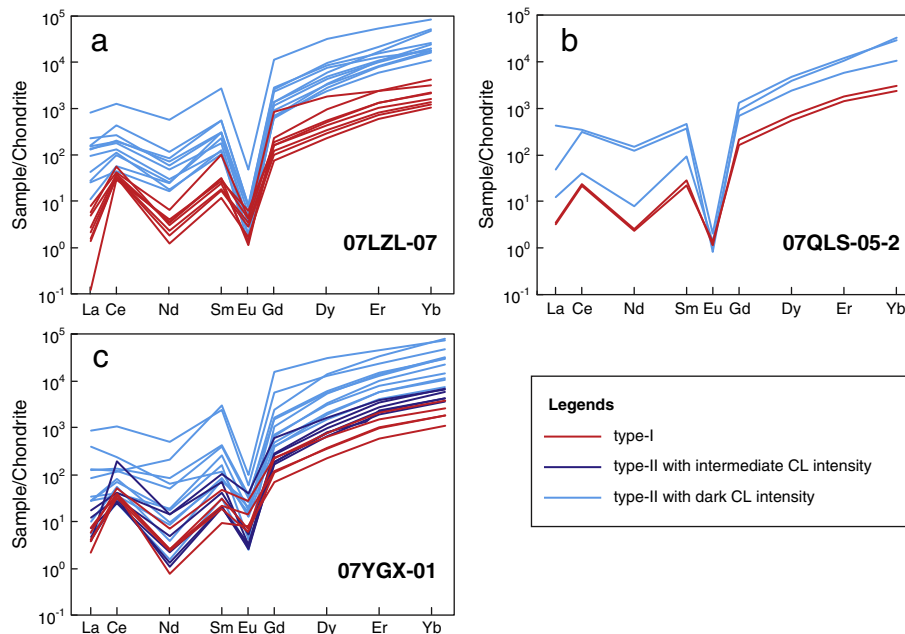

Fig. 6. Chondrite-normalized rare earth element patterns for Late Jurassic zircons from the Nanling area of southern China. Values for chondrites are from McDonough and Sun (1995). Type-II zircons generally have higher abundances of REEs and often have flatter LREEs relative to type-I zircons.
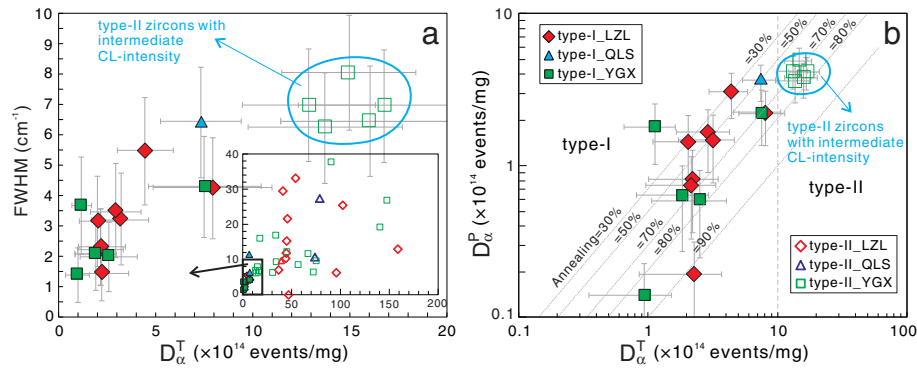
Fig. 7. Calculated total radiation damage D_α^T (if unannealed) *vs.* preserved damage D_α^P (laser Raman) of Late Jurassic zircons from the Nanling area of southern China. Error bars are shown as 2σ SE. Because domains with high FWHM are not suitable for calculating D_α^P (see text), only analyses with FWHM < 10 cm^{-1} are shown in the enlarged area of Fig. 7a and b. Type-II zircons with FWHM < 10 cm^{-1} (within the blue circles) belong to the domains with intermediate CL-intensity. (For interpretation of the references to color in this figure legend, the reader is referred to the web version of this article.)

zircons with intermediate CL-intensity follow this criteria, as shown in Fig. 7a. From Eq. (3), we can calculate the preserved D_α^P after annealing for type-I zircons as $0.01–0.37 \times 10^{15}$ α-decay events/mg, which is slightly lower than their accumulated dose from Eq. (2) ($D_\alpha^T = 0.1–0.79 \times 10^{15}$ α-decay events/mg) and suggests 30–70% of damage has been annealed for most type-I zircons (Fig. 7b). In contrast, type-II zircons with intermediate CL-intensity show a larger difference between D_α^T and D_α^P, suggesting that a higher percentage of the damage (67–76%) has been annealed (Fig. 7b).

4.2. Influence of radiation damage on U–Pb dating

Radiation damage could facilitate Pb mobility in zircons and thus commonly correlates with discordance of U–Pb ages (*e.g.*, Silver, 1991; Pidgeon et al., 1998a,b; Cherniak and Watson, 2000; Cherniak, 2010). Most commonly, mobility causes Pb loss from zircon domains, but it is also possible that Pb concentration could increase in local domains within a zircon. Such unsupported Pb could yield an erroneously old age, if not properly reintegrated during analysis (Valley et al., 2014). The correlation of Pb mobility and discordance on a Concordia plot (*e.g.*, Fig. 4) can be difficult to resolve for young (*e.g.*, <200 Ma) zircons that have experienced Pb loss because the calculated Pb/U ratios for these zircons plot on, or parallel to, the Concordia line and the large errors for some high-U analyses make calculations of concordance difficult to interpret. For example, the results of this study showed that most of the damaged type-II zircons are concordant in U–Pb isotopes (concordance = 90–110%) (Fig. 4) but are up to 70 Ma younger than the mean age (*ca.* 155 Ma) of type-I zircons. For these young zircons, the deviation from crystallization age is a better parameter to evaluate the influence of radiation damage. With increasing U concentration and deviation from crystallization age, Fe, and light-REE concentrations, and ^{16}OH/^{16}O in zircons also increase significantly (Figs. 5b, 6, S3, and Table S3).

Low-U type-I zircons show reproducible ^{206}Pb/^{238}U ages (*ca.* 155 Ma) with uncertainty of $\pm 3–5$ Ma (1SD) for individual analyses (Fig. 4; Table S3). In contrast, some type-II U–Pb ages vary from 80 to 160 Ma, and one (#QLS-2R1) is *ca.* 300 Ma (Fig. 3e; Table S3). Uncertainty for type-II zircons ranges from ± 1.5 to 18 Ma (1SD), with an average of ± 6 Ma. Similar to other type-II zircons, the older age of #QLS-2R1 is from a rim domain with dark CL intensity (Fig. S2b), precluding an inherited origin. The analysis has high common lead (16.7%), ~15,000 ppm U (Table S3), and is reversely discordant (Fig. 4), which is likely the result of matrix effects (discussed below) and Pb mobility causing an inaccurate common-Pb correction. The younger type-II dates could be explained in these two ways: (1) they represent the age of later fluid infiltration events; or (2) they resulted from Pb mobility (*e.g.*, Pb loss), possibly accompanied by SIMS matrix effects due to

radiation damage. If the first explanation is correct, type-II dates probably correspond to the ages of the associated W–Sn polymetallic mineralization. However, this explanation would require a prolonged (>60 Ma) period of hydrothermal activity, for which there is no geological evidence, and is inconsistent with previously published mica ^{40}Ar–^{39}Ar and molybdenite Re–Os isochron ages (Peng et al., 2006; Yuan et al., 2007) that are indistinguishable from type-I zircons ages within uncertainties. Furthermore, some high-U type-II zircons show U–Pb ages and oxygen isotope ratios consistent with type-I zircons (Fig. 3e). Therefore, the first explanation can be precluded. Pb mobility is the most likely explanation for younger or higher ^{206}Pb/^{238}U ages (Fig. 4).

Matrix effects (variation in sputtering and secondary ion yield attributed to differences in the composition of the target) differ for SIMS analysis of low-U *versus* high-U zircon domains, especially in areas that are metamict and no longer crystalline zircon. Variation in instrument (Pb$^+$/U$^+$) fractionation is typically calibrated against the measured UO$^+$/U$^+$ for each analysis, although other calibration approaches have been applied (*e.g.*, White and Ireland, 2012). This calibration cannot accurately account for differences in target compositions (*e.g.*, zircon *vs.* glass or metamict zircon). For this study, it is clear that the high U zircons do not behave the same way as the low U zircons (Fig. 8a), indicating different matrix effects. Williams and Hergt (2000) discussed matrix effects when they found that the ^{206}Pb/^{238}U ages of zircons from a 180 Ma Tasmanian dolerite are constant when U concentration is lower than 2500 ppm and increase with U concentrations above 2500 ppm (Fig. 8b). Likewise, a positive correlation of age and [U] is seen over a wide range of U concentrations for zircons from the Tasmanian dolerite (White and Ireland, 2012) (Fig. 8b) and in the granitic samples of Himalayan Leo Pargil Gneiss Dome (Leech, 2008). Localized gain of Pb in high-U damaged zircons along with variable matrix effects has also been noted (White and Ireland, 2012). However, no positive correlation was found for the high-U zircons from the *ca.* 155 Ma Nanling granites of this study (Fig. 8b).

At Nanling, ^{206}Pb/^{238}U ages decrease and become less reproducible when the U concentrations are higher than 8000 ppm, constituting a weak, negative correlation (Fig. 8b) with only one exception (#QLS-2R1). Such negative correlations could result from loss of radiogenic Pb (*e.g.*, Williams et al., 1984; Horie et al., 2006) or a localized gain of U in the zircon domain (*e.g.*, Grauert et al., 1974; Harrison et al., 1987) facilitated by radiation damage. We interpret the negative correlation of age and [U] for the Nanling zircons to be the result of Pb loss rather than gain of U because the ^{206}Pb/^{238}U ages are constant for a large range of U concentrations up to 8000 ppm (Fig. 8b). The analyses with the largest deviations in ^{206}Pb/^{238}U age from their inferred crystallization age generally show high iron concentrations and ^{16}OH/^{16}O (Fig. S3; Table S3), which provides additional evidence for open system behavior

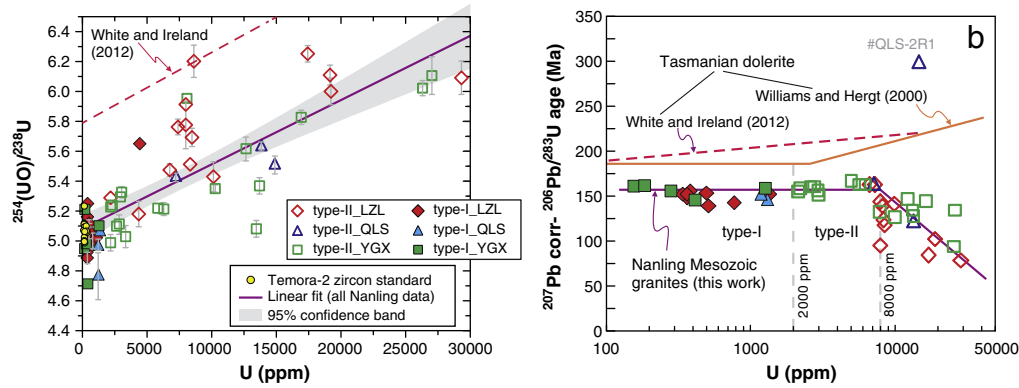**Fig. 8.** $^{254}(UO)/^{238}U$ (a) and U–Pb ages (b) *vs.* U concentrations ([U]). (a) There is a general correlation between $^{254}(UO)/^{238}U$ and [U] for high-U zircons. Error bars (1SD) for some analyses are smaller than symbol size. Type-I zircons have the same range of $^{254}(UO)/^{238}U$ values as the matrix matched Temora-2 standard (red dashed line, test2a from White and Ireland, 2012); (b) different trends occur between analyses from this study and zircons for Tasmanian dolerites (orange solid line, Williams and Hergt, 2000; red dashed line, White and Ireland, 2012). (For interpretation of the references to color in this figure legend, the reader is referred to the web version of this article.)

and element mobility facilitated by radiation damage (Pidgeon et al., 1998b; Rayner et al., 2005; Geisler et al., 2007).

The decreased reproducibility of type-II zircon is attributed to non-uniform sputtering efficiency of principally ^{238}U, ^{206}Pb, and ^{207}Pb from metamict zircon. This is reflected by large analytical uncertainties in the U–Pb and Pb–Pb ratios (Table S3), which may also reflect heterogeneously distributed Pb within the analytical volume (*e.g.*, Valley et al., 2014). Typically for young samples (<500 Ma), the $^{206}Pb/^{207}Pb$ age is imprecise because there is not enough radiogenic ^{207}Pb to measure accurately. For the high U Nanling zircons, the $^{206}Pb/^{207}Pb$ age is not count-rate limited and has the potential to be more precise than the $^{206}Pb/^{238}U$ age because Pb–Pb ages do not require a calibration (*i.e.*, UO^+/U^+ *vs.* Pb^+/U^+). However, despite the high concentration of radiogenic Pb for type-II zircons, the $^{206}Pb/^{207}Pb$ ages are as equally imprecise and inaccurate as U–Pb ages due to the non-uniform sputtering efficiency of heterogeneous, radiation-damaged zircon.

4.3. Influence of radiation damage on oxygen isotope ratios

Ion microprobe oxygen isotope analysis in zircon has been widely used to constrain source characteristics of magmas and degree of crustal melting (*e.g.*, Valley et al., 2005; Cavosie et al., 2007; Kemp et al., 2007; Moser et al., 2008; Wang et al., 2011, 2013). However, *in situ* oxygen isotope analysis requires detailed evaluation based on CL and SEM imaging because a number of factors can cause erroneous data, including radiation damage, micro-cracks, and inclusions (Valley et al., 1994; Valley, 2003; Cavosie et al., 2005; Grimes et al., 2011). When radiation damage accumulates in zircons, the resulting damaged crystal structure may have a different matrix effect during oxygen isotope analysis that cannot be corrected by use of the crystalline KIM-5 zircon standard. In extreme cases when zircons are fully metamict, standardization to a crystalline zircon is not valid, similar to U–Pb analyses. It is difficult to quantify how inaccurate measured oxygen values may be due to use of non-matrix matched standards, however, matrix-effects alone are unlikely to cause the 7‰ variation between type-I and type-II zircons.

For radiation-damaged zircons, micro-cracks and tiny inclusions are commonly developed, allowing secondary fluids to penetrate the damaged crystal. We have found that re-imaging analytical spots following SIMS oxygen isotope analysis is necessary, and subsequently, pits with tiny inclusions and cracks were excluded. In this work, it is noteworthy that some (n = 9) type-II zircons (especially domains with intermediate CL-intensity, up to 6000 ppm [U]) show $\delta^{18}O$ (>8.0‰) consistent with those of type-I zircons within uncertainty (Table 1; Fig. 9). The majority of type-II zircons (n = 22) do not have primary oxygen isotopic composition in equilibrium with the host melt recorded in type-I zircons (Fig. 9a). Moreover, a negative correlation is observed in the plots of $\delta^{18}O$ *vs.* U, Th and Y concentrations and total α-dose (Fig. 9a–

c, e). In particular, analyses of type-II domains of a single zircon grain can have different oxygen isotope ratios (Table 1). These data show that radiation damage has modified type-II zircons and played an important role in the alteration responsible for their wide range of $\delta^{18}O$ values. It should be noted that the threshold of [U] (=6000 ppm; Fig. 9a) for distinguishing the unaltered oxygen isotopes in this study is not generally applicable in other studies where zircons could have different ages and annealing histories. However, laser Raman provides an effective way to evaluate the amount of unannealed radiation damage, which impacts the preservation of oxygen isotope ratios (Fig. 9f).

Because addition of water is common during alteration, the amount of H in zircon could also be a measure of the amount of preserved radiation damage. This is also suggested by Pidgeon et al. (2013), who analyzed $^{16}OH/^{16}O$ without background correction in more highly altered zircons. The measured $^{16}OH/^{16}O$ values provide a relative monitor for water (or OH) content within the exact domain of zircon that was analyzed for $\delta^{18}O$. Fig. 10 shows that type-II zircons generally have more H (higher background-corrected $^{16}OH/^{16}O$) than type-I zircons (Table S1). The amount of H in type-II zircons is positively correlated with U, La and Fe concentrations and total cumulative α-decay dose, and H increases with decreasing Hf/Yb ratios, age, and $\delta^{18}O_{zircon}$ (Fig. 10). These correlations are reasonable because metamict zircon is known to contain water, but crystalline zircon is relatively H-free (Speer, 1982; Ewing et al., 2003; Geisler et al., 2003b,c; Utsunomiya et al., 2007; De Hoog et al., 2014). This provides a new and efficient way to evaluate radiation damage in zircons during SIMS oxygen isotope analysis. The ^{16}OH signal is measured at mass 17, which is generally an unused channel for terrestrial zircon analyses and is rarely reported or used for data interpretation. For this study, $\delta^{18}O_{zircon}$ values (mostly type-I zircons) have nearly constant corrected $^{16}OH/^{16}O$ below 0.0003. $\delta^{18}O$ values decrease in type-II zircons and correlate with increasing corrected $^{16}OH/^{16}O$ (Fig. 10e). This negative correlation is especially strong for sample 07LZL-07.

4.4. Formation of type-I and type-II zircons

A wide range of properties consistently distinguish type-I and type-II zircons. Type-I zircons are defined by the following: 1) bright oscillatory zonation in CL (Fig. 2 and S2); 2) low U, Th, REE, Fe, Ti and Y concentrations (Fig. 5; Table S3); and 3) reproducible and concordant U–Pb ages with low common Pb concentrations (Fig. 5; Table S3). In addition, low FWHM (Fig. 3c), high amplitude (Table S2) for B_{1g} laser Raman band, and low $^{16}OH/^{16}O$ ratios suggest that type-I zircons are primary and unaltered.

The average $\delta^{18}O$ value for type-I zircons (8.8 ± 0.5‰, 2SD) is elevated relative to typical mantle-like zircons ($\delta^{18}O_{zircon}$ = 5.3 ± 0.6‰, Valley et al., 2005), suggesting incorporation of supracrustal material into the magmatic protolith. This interpretation is consistent with the
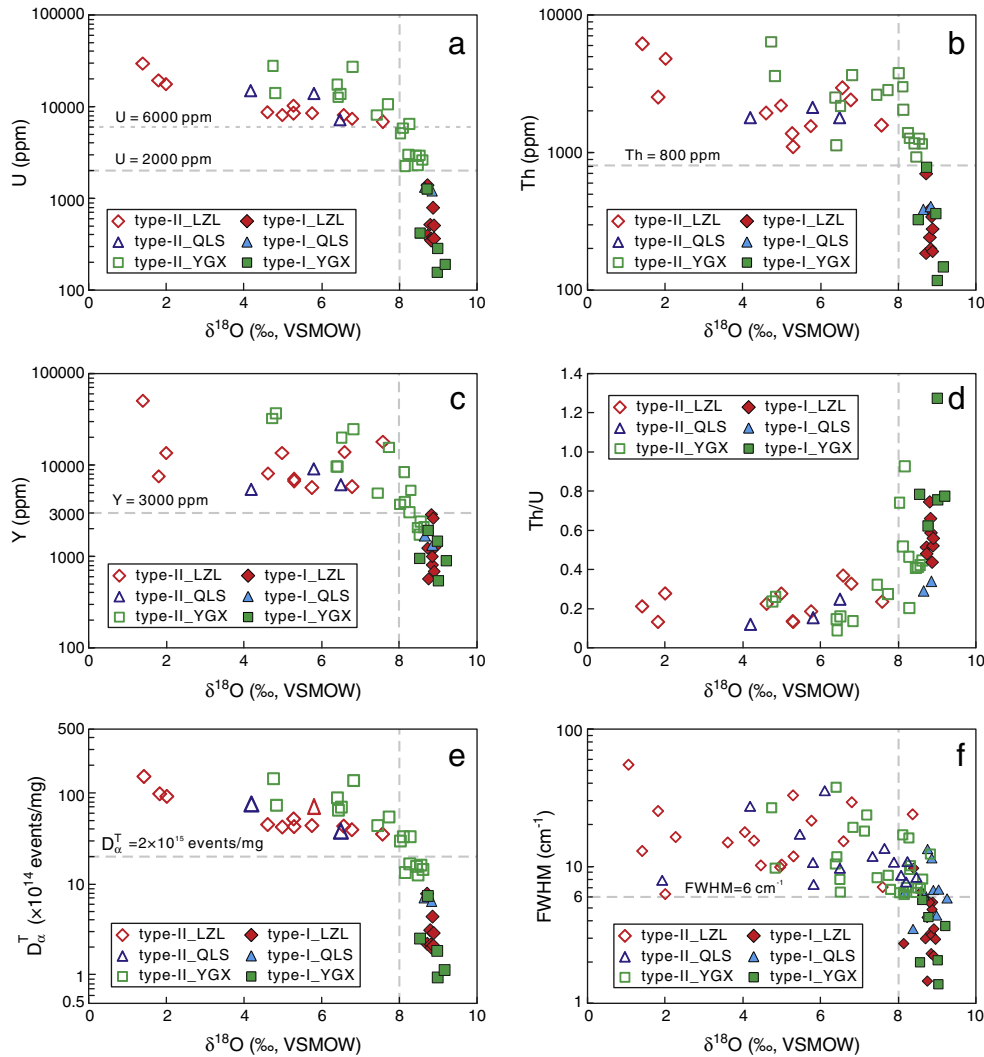
Fig. 9. (a–c) Trace elements, (d) Th/U, (e) total cumulative α-dose D_α^T, and (f) laser Raman FWHM *versus* δ18O plots for Late Jurassic zircons from the Nanling area of southern China showing the differences and correlations of δ18O values. The first percolation point for crystalline zircon (2×10^{15} α-decay events/mg; Ríos et al., 2000; Ewing et al., 2003) is indicated in panel e.

peraluminous compositions of the sample. Similar elevated δ18O values in zircons have also been reported in some Late Jurassic granites of the Nanling area, southern China, such as the *ca.* 160 Ma Xihuashan Pluton (9.0 ± 0.1‰, 2σ; Guo et al., 2012) and the *ca.* 160 Ma Fogang Pluton (high-δ18O endmember at 8–9‰; Li et al., 2009). The average δ18O$_{zircon}$ value (8.8‰) for type-I zircons in this study is equivalent to δ18O(WR) = 10.6‰ for the whole rock (WR) based on the average rock composition (71 wt.% SiO$_2$; Zhu et al., 2008) and the equation (Lackey et al., 2008):

$$\Delta^{18}O(WR-Zrc) \approx 0.0612 \times (SiO_2 \text{ wt.\%})_{WR} - 2.50‰. \quad (4)$$

If supracrustal Precambrian metasedimentary rocks (bulk δ18O = 11.9‰; Wang et al., 2013) in southern China were involved in the formation of the *ca.* 155 Ma Nanling granites, then the calculated high bulk oxygen isotope ratio (δ18O = 10.6‰) for the granites suggests a source composed of 80% supracrustal crust and 20% mantle-derived materials.

We note that some zircons are transitional between type-I and type-II. These zircons are identified as type-II, but have domains with intermediate CL intensity (Fig. S2; #3C, #4C, #10C, #13, #15C and #17C of 07YGX-01), moderate U (2000–3100 ppm) and Fe concentration (0.5–57 ppm), and relatively small age deviation (<10 Ma; most within 2σ uncertainties of type-I zircons) (Fig. 3e, S3; Table S3). Moreover, the transitional type-II

zircons generally have similar oxygen isotope ratios as type-I zircons and fall onto the chemical trends of type-I zircons (Fig. 9). Based on these observations, we suggest that type-II domains are variably altered, possibly representing deuteric zircons that grew as overgrowths around type-I domains or as individual grains during the later stage of magmatic evolution. U and Th concentrations were significantly elevated within some of the variably altered zircons, which promoted later radiation damage resulting in the altered type-II zircons showing reset ages and decreased δ18O values. The existence of variably altered zircon may be a common phenomenon in granitic bodies with high [U] and [Th], which locally may become increasingly enriched in these incompatible elements with increasing crystallization as the systems cools. In addition, shallow-level intrusions that cool relatively quickly and do not have a prolonged thermal history could permit unannealed radiation damage to accrue. Variably altered zircons may also be common in long-lived silicic magma chambers that cool to form partially solidified mush, which are later remobilized on eruption (*e.g.*, at Yellowstone; Bindeman et al., 2001).

5. Conclusions

Radiation damage can facilitate systematic alteration of zircon geochemistry. Identifying damage and quantifying the amount of damage are essential for interpretation of *in situ* measurements, including oxygen isotope ratios, trace elements, and U–Pb ages. The unusually large
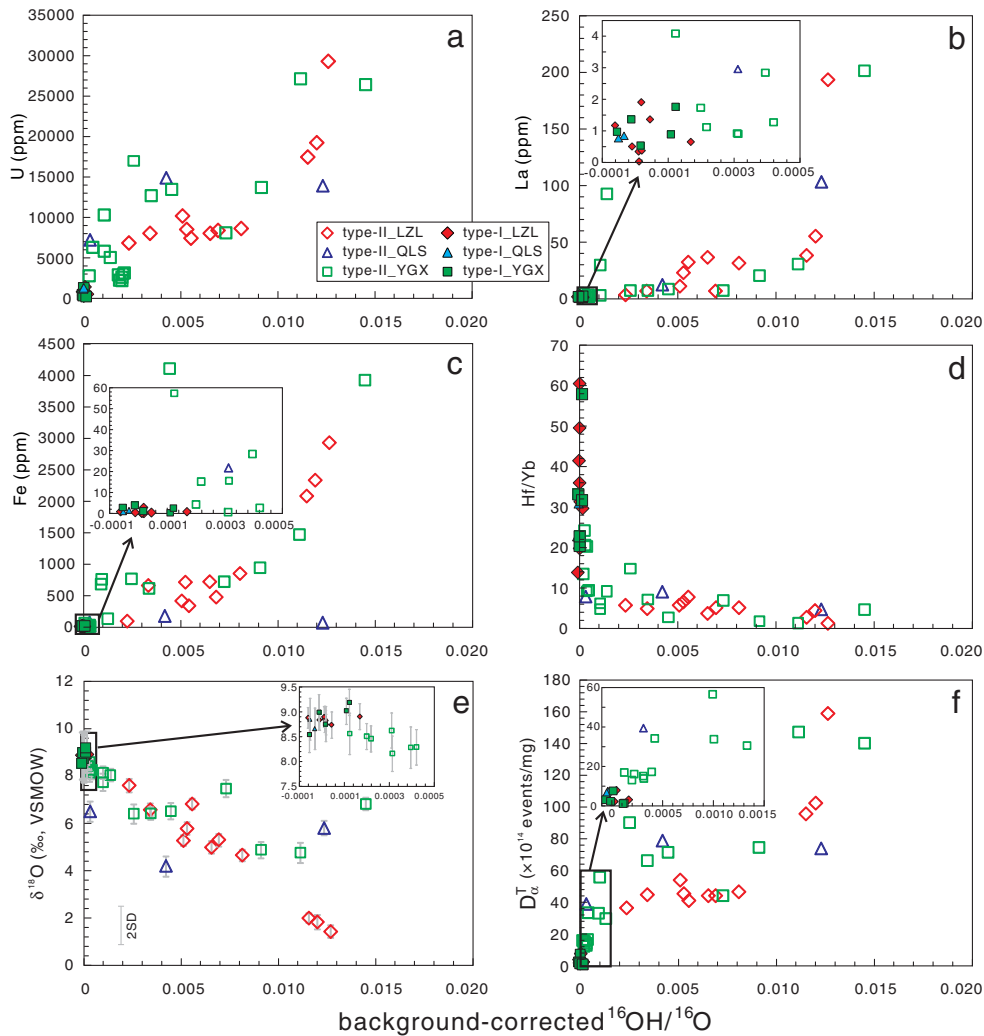
Fig. 10. Background-corrected $^{16}OH/^{16}O$ vs. (a) [U], (b) La, (c) Fe, (d) Hf/Yb, (e) $\delta^{18}O$, and (f) total dose D_α^T for Late Jurassic zircons from the Nanling area. The $^{16}OH/^{16}O$ values are a monitor for the amount of water in each zircon domain analyzed for $\delta^{18}O$ by SIMS.

variation of $\delta^{18}O$ from 1.4‰ to 8.6‰ in high-U–Th zircons from the ~155 Ma granites in the Nanling area of southern China is correlated with elevated and heterogeneous trace element concentrations including H. Broadening B_{1g} laser Raman band (FWHM), decreasing U–Pb age, and high cumulative α-dose indicate that these zircons are locally damaged by radiation. In contrast, the low-U–Th zircons are homogeneous in $\delta^{18}O$ with an average value of 8.8 ± 0.3‰ (2SD), low U, Th, REE and Fe concentrations, reproducible and concordant U–Pb ages, and low FWHM and high peak height for the Raman B_{1g} band. These results suggest that low-U–Th zircons are primary and magmatic grains that crystallized from granitic magmas. We interpret the high-U–Th grains as variably altered zircons that formed during late-stage magmatic evolution and that radiation damage accumulated later in high-U–Th grains. Radiation damage of high-U type-II zircons facilitated open system behavior, which caused Pb loss, inaccurate U–Pb ages, and lower $\delta^{18}O$ values. Additional uncertainty for U-rich domains can result from use of a non-matrix matched standard for SIMS analyses. This can strongly bias SIMS data, making the petrogenetic significance of U–Pb dates and $\delta^{18}O$ from high-U–Th zircons unreliable.

This study shows that the combined use of chemical indexes measured *in situ*, imaging, and laser Raman spectroscopy can effectively evaluate the reliability of U–Pb geochronology, oxygen isotopic data, processes of zircon crystallization, and the accumulation radiation damage. More importantly, background-corrected $^{16}OH/^{16}O$ value provides a new index for assessing radiation damage during SIMS analysis.

Supplementary data to this article can be found online at http://dx.doi.org/10.1016/j.chemgeo.2014.09.013.

References

Barth, A.P., Wooden, J.L., 2010. Coupled elemental and isotopic analyses of polygenetic zircons from granitic rocks by ion microprobe, with implications for melt evolution and the sources of granitic magmas. Chem. Geol. 277, 149–159.

Belousova, E.A., Griffin, W.L., O'Reilly, S.Y., 2006. Zircon crystal morphology, trace element signatures and Hf isotope composition as a tool for petrogenetic modeling: examples from Eastern Australian granitoids. J. Petrol. 47, 329–353.

Bindeman, I.N., Valley, J.W., Wooden, J.L., Persing, H.M., 2001. Post-caldera volcanism: in situ measurement of U–Pb age and oxygen isotope ratio in Pleistocene zircons from Yellowstone caldera. Earth Planet. Sci. Lett. 189, 197–206.

Black, L.P., Kamo, S.L., Allen, C.M., Davis, D.W., Aleinikoff, J.N., Valley, J.W., Mundil, R., Campbell, I.H., Korsch, R.J., Williams, I.S., Foudoulis, C., 2004. Improved $^{206}Pb/^{238}U$ microprobe geochronology by the monitoring of a trace-element-related matrix effect; SHRIMP, ID-TIMS, ELA-ICP-MS and oxygen isotope documentation for a series of zircon standards. Chem. Geol. 205, 115–140.

Bouvier, A.-S., Ushikubo, T., Kita, N.T., Cavosie, A.J., Kozdon, R., Valley, J.W., 2012. Li isotopes and trace elements as a petrogenetic tracer in zircon: insights from Archean TTGs and sanukitoids. Contrib. Mineral. Petrol. 163, 745–768.

Cavosie, A.J., Valley, J.W., Wilde, S.A., EIMF, 2005. Magmatic $\delta^{18}O$ in 4400–3900 Ma detrital zircons: a record of the alteration and recycling of crust in the Early Archean. Earth Planet. Sci. Lett. 235, 663–681.

Cavosie, A.J., Valley, J.W., Wilde, S.A., EIMF, 2006. Correlated microanalysis of zircon: trace element, $\delta^{18}O$, and U–Th–Pb isotopic constraints on the igneous origin of complex >3900 Ma detrital grains. Geochim. Cosmochim. Acta 70, 5601–5616.

Cavosie, A.J., Valley, J.W., Wilde, S., 2007. The oldest terrestrial mineral record: a review of 4400 to 4000 Ma detrital zircons from Jack Hills, Western Australia. In: Van Kranendonk, M.J., Smithies, R.H., Bennett, V.C. (Eds.), Earth's Oldest Rocks. Developments in Precambrian Geology 15, pp. 91–111.

Cherniak, D.J., 2010. Diffusion in accessory minerals: zircon, titanite, apatite, monazite and xenotime. Rev. Mineral. Geochem. 72, 827–869.

Cherniak, D.J., Watson, E.B., 2000. Pb diffusion in zircon. Chem. Geol. 172, 5–24.

Corfu, F., Hanchar, J.M., Hoskin, P.W.O., Kinny, P., 2003. Atlas of zircon textures. In: Hanchar, J.M., Hoskin, P.W.O. (Eds.), Zircon. Rev. Mineral. Geochem 53, pp. 469–500.

De Hoog, J.C.M., Lissenberg, C.J., Brooker, R.A., Hinton, R., Trail, D., Hellebrand, E., EIMF, 2014. Hydrogen incorporation and charge balance in natural zircon. Geochim. Cosmochim. Acta 141, 472–486.

Ewing, R.C., Meldrum, A., Wang, L., Weber, W.J., Corrales, L.R., 2003. Radiation effects in zircon. In: Hanchar, J.M., Hoskin, P.W.O. (Eds.), Zircon. Rev. Mineral. Geochem 53, pp. 378–420.

Farnan, I., Salje, E.K.H., 2001. The degree and nature of radiation damage in zircon observed by ^{29}Si nuclear magnetic resonance. J. Appl. Phys. 89, 2084–2090.

Farnan, I., Balan, E., Pickard, C.J., Mauri, F., 2003. The effect of radiation damage on local structure in the crystalline fraction of $ZrSiO_4$: investigating the ^{29}Si NMR response to pressure in zircon and reidite. Am. Mineral. 88, 1663–1667.

Fleischer, R.L., 2003. Etching of recoil tracks in solids. Geochim. Cosmochim. Acta 67, 4769–4774.

Fu, B., Page, F.Z., Cavosie, A.J., Fournelle, J., Kita, N.T., Lackey, J.S., Wilde, S.A., Valley, J.W., 2008. Ti-in-zircon thermometry: applications and limitations. Contrib. Mineral. Petrol. 156, 197–215.

Gao, Y.Y., Li, X.H., Griffin, W.L., O'Reilly, S.Y., Wang, Y.F., 2014. Screening criteria for reliable U–Pb geochronology and oxygen isotope analysis in uranium-rich zircons: a case study from the Suzhou A-type granites, SE China. Lithos 192–195, 180–191.

Garver, J.I., Kamp, P.J.J., 2002. Integration of zircon color and zircon fission-track zonation patterns in orogenic belts: application to the Southern Alps, New Zealand. Tectonophysics 349, 203–219.

Geisler, T., Pidgeon, R.T., Kurtz, R., Van Bronswijk, W., Schleicher, H., 2003a. Experimental hydrothermal alteration of partially metamict zircon. Am. Mineral. 88, 1496–1513.

Geisler, T., Rashwan, A.A., Rahn, M.K.W., Poller, U., Zwingmann, H., Pidgeon, R.T., Schleicher, H., Tomaschek, F., 2003b. Low temperature hydrothermal alteration of natural metamict zircons from the Eastern Desert, Egypt. Mineral. Mag. 67, 485–508.

Geisler, T., Zhang, M., Salje, E.K.H., 2003c. Recrystallization of almost fully amorphous zircon under hydrothermal conditions: an infrared spectroscopic study. J. Nucl. Mater. 320, 280–291.

Geisler, T., Burakov, B.E., Zirlin, V., Nikolaeva, L., Poml, P., 2005. A Raman spectroscopic study of high-uranium zircon from the Chernobyl "lava". Eur. J. Mineral. 17, 883–894.

Geisler, T., Schaltegger, U., Tomaschek, F., 2007. Re-equilibration of zircon in aqueous fluids and melts. Elem. 3, 43–50.

Grauert, B., Seitz, M.G., Soptrajanova, G., 1974. Uranium and lead gain of detrital zircon studies by isotopic analyses and fission-track mapping. Earth Planet Sci. Lett. 21, 389–399.

Grimes, C.B., Ushikubo, T., John, B.E., Valley, J.W., 2011. Uniformly mantle-like $\delta^{18}O$ in zircons from oceanic plagiogranites and gabbros. Contrib. Mineral. Petrol. 161, 13–33.

Guo, C.L., Chen, Y.C., Zeng, Z.L., Lou, F.S., 2012. Petrogenesis of the Xihuashan granites in southeastern China: constraints from geochemistry and in-situ analyses of zircon U–Pb–Hf–O isotopes. Lithos 148, 209–227.

Harrison, T.M., 2009. The Hadean crust: evidence from >4 Ga zircons. Annu. Rev. Earth Planet. Sci. 37, 479–505.

Harrison, T.M., Aleinikoff, J.N., Compston, W., 1987. Observations and controls on the occurrence of inherited zircon in Concord-type granitoids. Geochim. Cosmochim. Acta 51, 2549–2558.

Horie, K., Hidaka, H., Gauthier-Lafaye, F., 2006. Elemental distribution in zircon: alteration and radiation-damage effects. Phys. Chem. Earth 31, 587–592.

Hoskin, P.W.O., Schaltegger, U., 2003. The composition of zircon and igneous and metamorphic petrogenesis. In: Hanchar, J.M., Hoskin, P.W.O. (Eds.), Zircon. Rev. Mineral. Geochem 53, pp. 27–62.

Hu, R.Z., Zhou, M.F., 2012. Multiple Mesozoic mineralization events in South China—an introduction to the thematic issue. Miner. Deposita 47, 579–588.

Irmer, G., 1985. On the influence of the apparatus function on the determination of scattering cross sections and lifetime from optical phonon spectra. Experimentelle Technik der Physik 33, 501–506 (in German).

Kemp, A.I.S., Hawkesworth, C.J., Foster, G.L., Paterson, B.A., Woodhead, J.D., Hergt, J.M., Gray, C.M., Whitehouse, M.J., 2007. Magmatic and crustal differentiation history of granitic rocks from Hf–O isotopes in zircon. Science 315, 980–983.

Kita, N.T., Ushikubo, T., Fu, B., Valley, J.W., 2009. High precision SIMS oxygen isotope analyses and the effect of sample topography. Chem. Geol. 264, 43–57.

Krogh, T.E., Davis, G.L., 1975. Alteration in zircons and differential dissolution of altered and metamict zircon. Carnegie Inst. Washington, Year Book. 74, pp. 619–623.

Lackey, J.S., Valley, J.W., Chen, J.H., Stockli, D.F., 2008. Dynamic magma systems, crustal recycling, and alteration in the central Sierra Nevada batholiths: the oxygen isotope record. J. Petrol. 49 (7), 1397–1426.

Leech, M.L., 2008. Does the Karakoram fault interrupt mid-crustal channel flow in the western Himalaya? Earth Planet Sci. Lett. 276, 314–322.

Li, X.H., Li, X.W., Wang, X.C., Li, Q.L., Liu, Y., Tang, G.Q., 2009. Role of mantle-derived magma in genesis of early Yanshanian granites in the Nanling Range, South China: in situ zircon Hf–O isotopic constraints. Sci. China Ser. D 52 (9), 1262–1278.

Li, S.T., Wang, J.B., Zhu, X.Y., Wang, Y.L., Han, Y., Guo, N.N., 2011. Chronological characteristics of the Yaogangxian composite pluton in Hunan Province. Geol. Explor. 47 (2), 143–150 (in Chinese with English abstract).

Ludwig, K.R., 2009. SQUID 2, A User's Manual. 2. Berkeley Geochronology Center Special Publication, p. 100.

Ludwig, K.R., 2012. Isoplot 3.75, A Geochronological Toolkit for Excel. 5. Berkeley Geochronology Center Special, Publication, p. 75.

Marsellos, A.E., Garver, J.I., 2010. Radiation damage and uranium concentration in zircon as assessed by Raman spectroscopy and neutron irradiation. Am. Mineral. 95, 1192–1201.

McDonough, W.F., Sun, S.-S., 1995. The composition of the Earth. Chem. Geol. 120, 223–253.

Meldrum, A., Boatner, L.A., Weber, W.J., Ewing, R.C., 1998. Radiation damage in zircon and monazite. Geochim. Cosmochim. Acta 62, 2509–2520.

Moser, D.E., Bowman, J.R., Wooden, J., Valley, J.W., Mazdab, F., Kita, N., 2008. Creation of a continent recorded in zircon zoning. Geology 36, 239–242.

Muñoz, M., Charrier, R., Fanning, C.M., Maksaev, V., Deckart, K., 2012. Zircon trace element and O–Hf Isotope analyses of mineralized intrusions from El Teniente ore deposit, Chilean Andes: constraints on the source and magmatic evolution of porphyry Cu–Mo related magmas. J. Petrol. 53 (6), 1091–1122.

Murakami, T., Chakoumakos, B.C., Ewing, R.C., Lumpkin, G.R., Weber, W.J., 1991. Alpha-decay event damage in zircon. Am. Mineral. 76, 1510–1532.

Nasdala, L., Pidgeon, R.T., Wolf, D., Irmer, G., 1998. Metamictization and U–Pb isotopic discordance in single zircons: a combined Raman microprobe and SHRIMP ion probe study. Mineral. Petrol. 62, 1–27.

Nasdala, L., Wenzel, M., Vavra, G., Irmer, G., Wenzel, T., Kober, B., 2001. Metamictisation of natural zircon: accumulation versus thermal annealing of radioactivity-induced damage. Contrib. Mineral. Petrol. 141, 125–144.

Nasdala, L., Reiners, P.W., Garver, J.I., Kennedy, A.K., Stern, R.A., Balan, E., Wirth, R., 2004. Incomplete retention of radiation damage in zircon from Sri Lanka. Am. Mineral. 89, 219–231.

Nasdala, L., Miletich, R., Ruschel, K., Váczi, T., 2008. Raman study of radiation-damaged zircon under hydrostatic compression. Phys. Chem. Miner. 35, 597–602.

Orland, I.J., 2012. Seasonality From Speleothems: High-resolution Ion Microprobe Studies at Soreq Cave, Israel (Doctoral dissertation) University of Wisconsin-Madison.

Palenik, C.S., Nasdala, L., Ewing, R.C., 2003. Radiation damage in zircon. Am. Mineral. 88, 770–781.

Peck, W.H., Valley, J.W., Wilde, S., Graham, C.M., 2001. Oxygen isotope ratios and rare earth elements in 3.3 to 4.4 Ga zircons: ion microprobe evidence for high $\delta^{18}O$ continental crust and oceans in the Early Archean. Geochim. Cosmochim. Acta 65, 4215–4229.

Peng, J.T., Zhou, M.F., Hu, R.Z., Shen, N.P., Yuan, S.D., Bi, X.W., Du, A.D., Qu, W.J., 2006. Precise molybdenite Re–Os and mica Ar–Ar dating of the Mesozoic Yaogangxian tungsten deposit, central Nanling district, South China. Miner. Deposita 41, 661–669.

Pidgeon, R.T., Nasdala, L., Todt, W., 1998a. Determination of radiation damage ages on parts of zircon grains by Raman microprobe: implications for annealing history and U–Pb stability. Mineral. Mag. 62A, 1174–1175.

Pidgeon, R.T., Nemchin, A.A., Hitchen, G.J., 1998b. Internal structures of zircons from Archean granites from the Darling Range batholith: implications for zircon stability and the interpretation of zircon U–Pb ages. Contrib. Mineral. Petrol. 132, 288–299.

Pidgeon, R.T., Nemchin, A.A., Cliff, J., 2013. Interaction of weathering solutions with oxygen and U–Pb isotopic systems of radiation-damaged zircon from an Archean granite, Darling Range Batholith, Western Australia. Contrib. Mineral. Petrol. 166, 511–523.

Qi, H.W., Hu, R.Z., Wang, X.F., Qu, W.J., Bi, X.W., Peng, J.T., 2012. Molybdenite Re–Os and muscovite $^{40}Ar/^{39}Ar$ dating of quartz vein-type W–Sn polymetallic deposits in Northern Guangdong, South China. Miner. Deposita 47, 607–622.

Rayner, N., Stern, R.A., Carr, S.D., 2005. Grain-scale variations in trace element composition of fluid-altered zircon, Acasta Gneiss Complex, northwestern Canada. Contrib. Mineral. Petrol. 148, 721–734.

Ríos, S., Salje, E.K.H., Zhang, M., Ewing, R.C., 2000. Amorphization in zircon: evidence from direct impact damage. J. Phys. Condens. Matter 12, 2401–2412.

Shen, W.Z., Wang, D.Z., Xie, Y.L., Liu, C.S., 1995. Geochemical characteristics and material sources of the Qianlishan composite granite body, Hunan Province. Acta Petrol. Mineral. 14 (3), 193–202.

Shu, X.J., Wang, X.L., Sun, T., Dai, M.N., 2011. Zircon trace elements, U–Pb ages and Hf isotopes for the Mesozoic granites from the western Nanling Range, South China: implication for petrogenesis and W–Sn mineralization. Lithos 127, 468–482.

Shu, X.J., Wang, X.L., Sun, T., Chen, W.F., Shen, W.Z., 2013. Crustal formation in the Nanling Range, South China Block: Hf isotope evidence of zircons from Phanerozoic granitoids. J. Asian Earth Sci. 74, 210–224.

Silver, L.T., 1991. Daughter–parent isotope systematics in U–Th bearing igneous accessory mineral assemblages as potential indices of metamorphic history: a discussion of the

concept. In: Taylor, H.P., et al. (Eds.), Stable Isotope Geochemistry: A Tribute to Samuel Epstein. Geochem. Soc. Spec. Publ. 3, pp. 391–407.

Sinha, A.K., Wayne, D.M., Hewitt, D.A., 1992. The hydrothermal stability of zircon: preliminary experimental and isotopic studies. Geochim. Cosmochim. Acta 56, 3551–3560.

Speer, J.A., 1982. 2nd ed. Zircon. Rev. Mineral 5, pp. 67–112.

Stacey, J., Kramers, J.D., 1975. Approximation of terrestrial lead isotope evolution by a two-stage model. Earth Planet. Sci. Lett. 26, 207–221.

Steely, A.N., Hourigan, J.K., Juel, E., 2014. Discrete multi-pulse laser ablation depth profiling with a single-collector ICP-MS: sub-micron U–Pb geochronology of zircon and the effect of radiation damage on depth-dependent fractionation. Chem. Geol. 372, 92–108.

Trachenko, K.O., Dove, M.T., Salje, E.K.H., 2001. Atomistic modeling of radiation damage in zircon. J. Phys. Condens. Matter 13, 1947–1959.

Ushikubo, T., Kita, N.T., Cavosie, A.J., Wilde, S.A., Rudnick, R.L., Valley, J.W., 2008. Lithium in Jack Hills zircons: evidence for extensive weathering of Earth's earliest crust. Earth Planet. Sci. Lett. 272, 666–676.

Utsunomiya, S., Valley, J.W., Cavosie, A.J., Wilde, S.A., Ewing, R.C., 2007. Radiation damage and alteration of zircon from a 3.3 Ga porphyritic granite from the Jack Hills, Western Australia. Chem. Geol. 236, 92–111.

Valley, J.W., 2003. Oxygen isotopes in zircon. Rev. Mineral. Geochem. 53, 343–385.

Valley, J.W., Kita, N.T., 2009. In situ oxygen isotope geochemistry by ion microprobe. In: Fayek, M. (Ed.), MAC Short Course: Secondary Ion Mass Spectrometry in the Earth Sciences vol 41. Mineralogical Association of Canada, Quebec, pp. 19–63.

Valley, J.W., Chiarenzelli, J.R., McLelland, J.M., 1994. Oxygen isotope geochemistry of zircon. Earth Planet. Sci. Lett. 126, 187–206.

Valley, J.W., Lackey, J.S., Cavosie, A.J., Clechenko, C.C., Spicuzza, M.J., Basei, M.A.S., Bindeman, I.N., Ferreira, V.P., Sial, A.N., King, E.M., Peck, W.H., Sinha, A.K., Wei, C.S., 2005. 4.4 billion years of crustal maturation: oxygen isotopes in magmatic zircon. Contrib. Mineral. Petrol. 150, 561–580.

Valley, J.W., Cavosie, A.J., Ushikubo, T., Reinhard, D.A., Lawrence, D.F., Larson, D.J., Clifton, P.H., Kelly, T.F., Wilde, S.A., Moser, D.E., Spicuzza, M.J., 2014. Atom-probe tomography and nano-geochronology of a Hadean post-magma–ocean zircon. Nat. Geosci. 7, 219–223.

Wang, X.C., Li, Z.X., Li, X.H., Li, Q.L., Tang, G.Q., Zhang, Q.R., Liu, Y., 2011. Nonglacial origin for low-δ^{18}O Neoproterozoic magmas in the South China Block: evidence from new in-situ oxygen isotope analyses using SIMS. Geology 39, 735–738.

Wang, X.L., Zhou, J.C., Wan, Y.S., Kitajima, K., Wang, D., Bonamici, C., Qiu, J.S., Sun, T., 2013. Magmatic evolution and crustal recycling for Neoproterozoic strongly peraluminous granitoids from southern China: Hf and O isotopes in zircon. Earth Planet. Sci. Lett. 366, 71–82.

Watson, E.B., Wark, D.A., Thomas, J.B., 2006. Crystallization thermometers for zircon and rutile. Contrib. Mineral. Petrol. 151, 413–433.

Weber, W.J., Ewing, R.C., Wang, L.-M., 1994. The radiation-induced crystal-line-to-amorphous transition in zircon. J. Mater. Res. 9, 688–698.

White, L.T., Ireland, T.R., 2012. High-uranium matrix effect in zircon and its implications for SHRIMP U–Pb age determinations. Chem. Geol. 306–307, 78–91.

Williams, I.S., Hergt, J.M., 2000. U–Pb dating of Tasmanian dolerites: a cautionary tale of SHRIMP analysis of high-U zircon. In: Woodhead, J.D., Hergt, J.M., Noble, W.P. (Eds.), Beyond 2000: New Frontiers in Isotope Geoscience: Lorne, pp. 185–188 (Abstract Proceedings).

Williams, I.S., Compston, W., Black, L.P., Ireland, T.R., Foster, J.J., 1984. Unsupported radiogenic Pb in zircon: a cause of anomalously high Pb–Pb, U–Pb and Th–Pb ages. Contrib. Mineral. Petrol. 88, 322–327.

Xu, X.S., Zhang, M., Zhu, K.Y., Chen, X.M., He, Z.Y., 2012. Reverse age zonation of zircon formed by metamictisation and hydrothermal fluid leaching. Lithos 150, 256–267.

Yuan, S.D., Peng, J.T., Shen, N.P., Hu, R.Z., Dai, T.M., 2007. ^{40}Ar–^{39}Ar isotopic dating of the Xianghualing Sn-polymetallic orefield in southern Hunan, China and its geological implications. Acta Geol. Sin. 81 (2), 278–286.

Zhang, M., Salje, E.K.H., Ewing, R.C., Ríos, S., Schlüter, J., Leggo, P., 2000. Alpha-decay damage and recrystallization in zircon: evidence for an intermediate state from infrared spectroscopy. J. Phys. Condens. Matter 12, 5189–5199.

Zhou, X.M., Sun, T., Shen, W.Z., Shu, L.S., Niu, Y.L., 2006. Petrogenesis of Mesozoic granitoids and volcanic rocks in South China: a response to tectonic evolution. Episodes 29 (1), 26–33.

Zhu, J.C., Chen, J., Wang, R.C., Lu, J.J., Xie, L., 2008. Early Yanshanian NE trending Sn/W-bearing A-type granites in the western-middle part of the Nanling Mts Region. Geol. J. China Univ. 14 (4), 474–484 (in Chinese with English abstract).

Zhu, J.C., Wang, R.C., Lu, J.J., Zhang, H., Zhang, W.L., Xie, L, Zhang, R.Q., 2011. Fractionation, evolution, petrogenesis and mineralization of Laiziling granite pluton, southern Hunan Province. Geol. J. China Univ. 17 (3), 381–392 (in Chinese with English abstract).